Journal of Nanobiotechnology

RESEARCH Open Access

3D printed porous magnesium metal scaffolds with bioactive coating for bone defect repair: enhancing angiogenesis and osteogenesis

Jianting Ye[1†], Bozun Miao[2†], Yingjie Xiong[1†], Yanjun Guan[1], Yuzheng Lu[1,3], Zhibo Jia[1,4], Yanbin Wu[1], Xiaohan Sun[1], Congcong Guan[1,5], Ruichao He[1,5], Xing Xiong[1], Huihui Jia[1], Hongyu Jiang[1], Zexian Liu[1], Yuxuan Zhang[1,6], Yu Wei[1], Wancheng Lin[1,3], Aiyuan Wang[1], Yu Wang[1], Haoye Meng[1], Wenjing Xu[1], Guangyin Yuan[2*] and Jiang Peng[1*]

Abstract

In orthopedics, the effective treatment of bone defects remains a major challenge. Magnesium (Mg) metals, with their excellent biocompatibility and favorable osteoconductivity, osteoinductivity, and osseointegration properties, hold great promise for addressing this issue. However, the rapid degradation rate of magnesium restricts its clinical application. In this study, a triply periodic minimal surface (TPMS)-structured porous magnesium alloy (Mg-Nd-Zn-Zr, JDBM) was fabricated using the laser powder bed fusion (LPBF) process. Strontium-doped octacalcium phosphate (SrOCP) and strontium hydrogen phosphate biphasic composite coatings were applied to the surface of the scaffolds. The results showed that the TPMS structure exhibited porous biomimetic characteristics that resemble cancellous bone, promoting vascular ingrowth and new bone formation. Additionally, the SrOCP coating significantly increased the surface roughness and hydrophilicity of the scaffold, which enhanced cell adhesion and osteogenic differentiation. The SrOCP coating also markedly reduced the degradation rate of the JDBM scaffolds while ensuring the sustained release of bioactive ions (Mg^{2+}, Zn^{2+}, Sr^{2+}, and Ca^{2+}), thus maintaining the scaffolds' biofunctional activity. Compared to JDBM scaffolds, JDBM/SrOCP scaffolds exhibited better biocompatibility and stronger vascularization and bone regeneration capabilities both in vitro and in vivo. Overall, this study presents a novel strategy for the repair of bone defects using magnesium-based biomaterials, providing new insights for future clinical applications.

Introduction

The number of patients suffering from bone defects caused by multiple illnesses, including Osteoporosis (OP), trauma, infection, and tumor resection, is gradually increasing with the aging population [1, 2]. Musculoskeletal disorders resulting from the aforementioned causes impose an estimated annual burden of $136.8 billion in the United States [3]. Despite significant advances in medical treatments, the effective treatment of bone defects remains a major challenge for both patients and orthopedic surgeons worldwide [4]. Autologous bone grafting [5] is the gold standard for treating bone defects,

†Jianting Ye, Bozun Miao and Yingjie Xiong contributed equally to this work.

*Correspondence:
Guangyin Yuan
gyyuan@sjtu.edu.cn
Jiang Peng
pengjiang301@126.com

Full list of author information is available at the end of the article

Graphical abstract

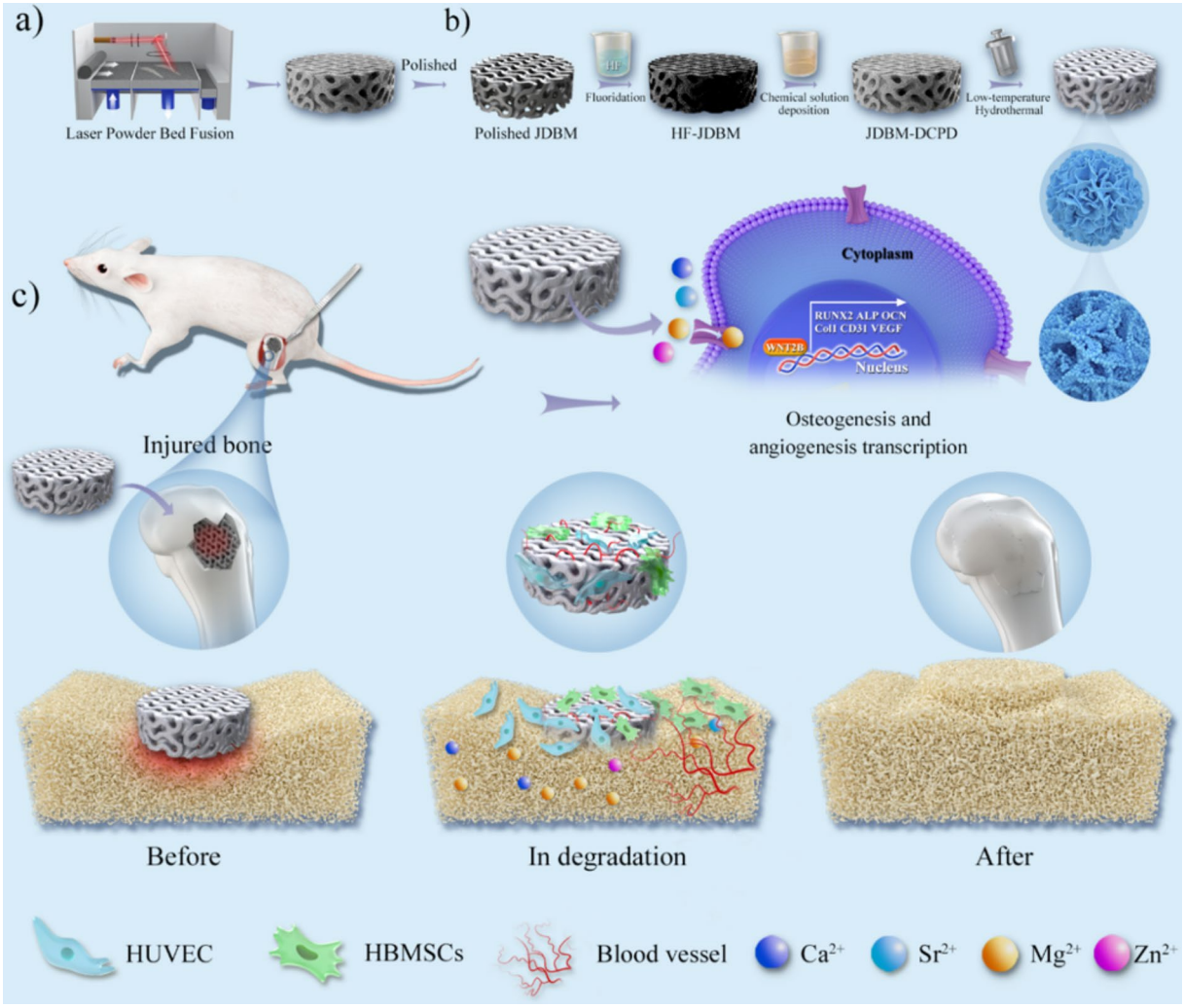

Keywords 3D printing, Biodegradable magnesium alloy, Nanocomposite coating, Neovascularization, Bone regeneration

with over 2 million patients undergoing the procedure annually. However, its clinical application is highly restricted by limitations in natural bone sources [6], as well as structural and vascular damage at donor sites. Furthermore, although allogeneic bone [7] transplantation could somewhat alleviate the shortage of bones, immune rejection and potentially pathogenic bacteria remain significant causes of surgical failure [8, 9]. On the other hand, although bioceramic materials [9] have gained considerable attention due to their favorable biocompatibility, their brittleness and other drawbacks hinder their widespread clinical adoption. Metal materials [10] commonly used in clinical practice, such as stainless steel, titanium, and tantalum, have also demonstrated good biosafety while providing stable mechanical support for bone defect areas, but these non-degradable materials possess high elastic moduli, making them highly susceptible to stress shielding and secondary fracture risks [11]. Specifically, external forces could lead to complications such as implant loosening or resorption of surrounding tissues or even adjacent bones around implants [12]. Therefore, developing suitable alternative biomaterials for clinical applications in repairing bone defects is imperative.

An ideal material [13] for repairing bone defects should possess biomimetic characteristics [14], specifically a biomimetic structure [15] and an appropriate microenvironment [16]. In other words, to facilitate blood vessel ingrowth and new bone formation [17], the biomimetic repair material should have pore sizes and porosity [18]

comparable to those of natural bone. The repair process of bone defects is primarily governed by the local microenvironment [16], which plays a central role throughout the healing process. An osteogenic and angiogenic microenvironment is crucial for successful bone defect repair. Therefore, biomimicking the local microenvironment is of particular importance [16, 19].

Magnesium ion (Mg^{2+}), the fourth most abundant cation in the human body [20], participates in numerous biochemical reactions and is a fundamental element in bone composition. Healthy adults require a daily intake of 310–420 mg of magnesium to maintain normal body function [21]. Moreover, Mg^{2+} possesses distinct biosafety advantages over other metals. Extensive research has demonstrated [22, 23] that Mg^{2+} released during the degradation of magnesium metals or alloys could promote angiogenesis and facilitate new bone formation, among other biological functionalities [24]. Notably, Mg^{2+} exhibits biological properties comparable to growth factors like Bone Morphogenetic Protein-2 (BMP-2) [25] and could effectively mitigate the risks associated with ectopic bone formation or growth factor-induced tumor induction. Furthermore, magnesium metals or alloys [26] possess excellent osseointegration properties, enabling rapid integration into surrounding tissues. Additionally, among all metallic materials, the Young's modulus and compressive strength of magnesium metals or alloys [27] closely resemble those of natural bone, implying that they could provide stable mechanical properties, preventing stress shielding and secondary fractures. Consequently, magnesium metal is a highly promising candidate for clinical translation as a metallic biomaterial.

However, the rapid degradation rate of magnesium metal results in substantial localized accumulation of Mg^{2+} and hydrogen production [28, 29] within a short period, creating an alkaline environment with a high Mg^{2+} concentration. Besides significantly hindering cell proliferation, this increased local Mg^{2+} concentration and the resulting alkaline environment also impede the formation of new bones and blood vessels. Moreover, hypermagnesemia [30] can lead to severe complications such as neuromuscular paralysis and cardiac arrest, thereby diminishing the biosafety and activity of magnesium metal. Therefore, discovering avenues for inhibiting the rapid degradation of magnesium metal is vital for its clinical application.

The modification of magnesium metal is a crucial research area. There have been many relevant studies on the modification of magnesium metal. For example, Qin et al. [31] added magnesium particles to PLGA and PCL polymer materials and employed three-dimensional (3D) printing to prepare porous scaffolds with excellent biosafety and osteogenic abilities. Although these scaffolds could sustain Mg^{2+} release, they exhibited poor mechanical properties and were unsuitable for bone defect repair at weight-bearing sites. Furthermore, magnesium and many other related alloys, mainly magnesium-calcium [32], magnesium-zinc [33], and magnesium-aluminum [34], among others [35], have been examined for many years. These alloys have demonstrated good biocompatibility and osteogenic performance, and their degradation rates have been somewhat effectively controlled. However, high concentrations of ions in the degradation products of some of these alloys necessitate further investigation of their biosafety. Furthermore, the alloying strategy has not fully addressed the rapid degradation rate of magnesium. The introduction of bioactive coatings [36, 37] on the surface of magnesium metals to further reduce their degradation rate has recently shown promising results. Some of these coatings included calcium-phosphorus [38], zinc-phosphorus [39], and magnesium-phosphorus [40], which have gained significant research attention due to their excellent corrosion resistance properties. Yan et al. [41] compared the calcium-phosphorus coating with the strontium-phosphorus coating and found that although they possessed comparable corrosion resistance properties, the latter showed better biofunctionality. Therefore, the introduction of the strontium element may provide a novel direction for research on magnesium metal coatings.

This study aims to develop a dual-biomimetic porous material that mimics both the physical structure and the physiological microenvironment of natural bone. Specifically, we fabricated a TPMS-structured Jiao Da Bio-Magnesium(JDBM) porous magnesium alloy scaffold using the Laser Powder Bed Fusion (LPBF) 3D printing process. A Ca-P coating was in situ deposited on the surface through chemical deposition, while biologically active strontium was innovatively introduced. The Ca-P coating was hydrothermally transformed into a uniform, dense dual-phase composite nanocoating structure comprising a Strontium-doped Octacalcium Phosphate (Sr-OCP) and strontium hydrogen phosphate. The goal was to explore the applicability of composite nanobioactive-coated porous magnesium alloy scaffolds (JDBM/SrOCP) in bone defect regeneration. Additive manufacturing could reproduce the physical structure of natural bone (mimicking its porosity and pore size), enabling neovascularization and new bone formation. We hypothesize that SrOCP nano-bioactive coatings could further reduce the degradation rate of magnesium metal. At the same time, the SrOCP nano-bioactive coating increases the surface area and roughness of the magnesium scaffolds, providing numerous attachment points and biological sites for the cells. During the regeneration process, this surface structure facilitates the cell-scaffold interaction.This study systematically investigated the

properties of the 3D-printed porous magnesium metal scaffolds(Video) with composite nanobioactive coatings both in vitro and in vivo. The scaffolds were characterized using Scanning Electron Microscopy (SEM), Energy Dispersion Spectroscopy (EDS), X-ray Diffraction (XRD), Atomic Force Microscopy (AFM), a Contact Angle (CA) goniometer, and Inductively Coupled Plasma Emission Spectroscopy (ICP-OES). The biocompatibility and biological functionality of the scaffolds were assessed in vitro using Human Bone Marrow Mesenchymal Stem Cells (HBMSCs) and Human Umbilical Vein Endothelial Cells (HUVECs). Finally, both scaffolds' osteogenic and angiogenic capabilities were confirmed using a Sprague Dawley (SD) rat femoral condyle bone defect model.

Results

Construction and characterization of biomimetic scaffolds

In this study, the TPMS-structured porous magnesium alloys prepared via the LPBF process exhibited both structural and functional dual-biomimetic properties (Fig. 1A). The structural parameters are shown in Table 1. The JDBM and JDBM/SrOCP scaffolds had pore diameters of 728.57 ± 12.64 μm and 666.39 ± 13.39 μm, respectively, with corresponding porosities of 72.08 ± 1.26% and 65.58 ± 1.69%. Both scaffolds were highly interconnected, with 100% connectivity (Table 1). Regarding the mechanical results, compared to the JDBM scaffold, the JDBM/SrOCP scaffold (Fig. 1B-D) exhibited superior compressive strength [(59.81 ± 0.83) MPa vs. (42.07 ± 0.27) MPa] and Young's modulus [(0.91 ± 0.08) GPa vs. (0.81 ± 0.04) GPa], demonstrating that the composite coating did not affect the scaffold's mechanical properties.

Furthermore, SEM and EDS analyses revealed that the JDBM scaffold had a smooth surface with no observable metal particles, confirming its integrity (Fig. 1E-F, Fig. S1, Supporting Information 1). Magnesium, neodymium, zinc, and zirconium were uniformly distributed on the scaffold's surface, with magnesium exhibiting the highest content. On the other hand, the JDBM/SrOCP scaffold had a rough surface with uniformly distributed microspheres self-assembled from nanoparticles (NPs). Calcium, phosphorus, strontium, and magnesium were also uniformly distributed on this surface, with calcium and phosphorus showing higher levels. XRD analysis confirms that the preparation method for the JDBM/SrOCP scaffold coating is correct (Supplementary Material 1, Fig. S4).The porous magnesium metal scaffolds were examined before and after surface modification using AFM and CA techniques (Fig. 1G-I). According to the results, JDBM/SrOCP scaffolds had a significantly higher surface roughness than JDBM scaffolds. Additionally, JDBM/SrOCP scaffolds had a notably smaller water contact angle than JDBM scaffolds and showing improved surface hydrophilicity. These findings collectively suggest that the composite coatings increased the scaffold's surface area and enhanced the cell adhesion environment.

In vitro degradation behavior of biomimetic scaffolds

The scaffolds' degradation behavior was further evaluated using immersion experiments. The pH tests revealed that both scaffolds exhibited an upward trend in pH levels during the initial stage of immersion (Fig. 2A). Notably, the extract from the JDBM scaffold showed the most rapid increase, reaching a pH of 9.5 on the first day and over 10 by the fifth day, respectively, and thereafter maintained a gradual rise. On the other hand, the JDBM/SrOCP scaffold showed a slight increase in pH during its early stage, which consistently remained below 9.5 afterward and gradually decreased in the later stages. Regarding the ion release rate (Fig. 2B-E), Mg^{2+} was explosively released from the JDBM scaffold during its initial phase, with nearly half of the total release occurring within three days. The release rate slowed down in the subsequent days. On the other hand, the JDBM/SrOCP scaffold exhibited a significantly lower Mg^{2+} release rate within the first three days at ~ 10% of the total release. Although the JDBM/SrOCP scaffold had a slight upward trend in the Mg^{2+} release rate in the subsequent days, it remained considerably lower than that of the JDBM scaffold.

Furthermore, Ca, Sr, and P exhibited a comparable release rate trend from the JDBM/SrOCP porous scaffold during degradation (Fig. 2D, E). The scaffold exhibited a rapid initial release rate within the first three days, followed by a gradual slowdown. Figure 2C shows the remaining mass percentages of the JDBM and JDBM/SrOCP scaffolds. After two weeks of immersion experiments, JDBM scaffolds retained ~ 50% of their original mass, whereas JDBM/SrOCP scaffolds lost only ~ 10%. The scaffolds' surface composition and morphological characteristics post-immersion were visualized using XRD and SEM. The XRD results showed that hydroxyapatite-like substances mainly dominated the surface products of JDBM/SrOCP scaffolds post-immersion, whereas magnesium hydroxide and other substances mainly dominated the surface of JDBM scaffolds post-immersion (Fig. 2F, Supporting Information 1, Fig. S5). The SEM results (Fig. 2G, Supporting Information 1, Fig. S2) revealed numerous cracks and columnar crystals on the surface of the JDBM scaffold. On the other hand, EDS analysis revealed a uniform distribution of elements on the JDBM scaffold's surface, primarily comprising magnesium. Although JDBM/SrOCP scaffolds did not have significant cracks and were still covered with a micro-nanocomposite coating on the surface, EDS analysis showed a uniform distribution of various elements including Sr, Ca, P, Mg, and other elements on their surface, with Ca and P having the highest content. These

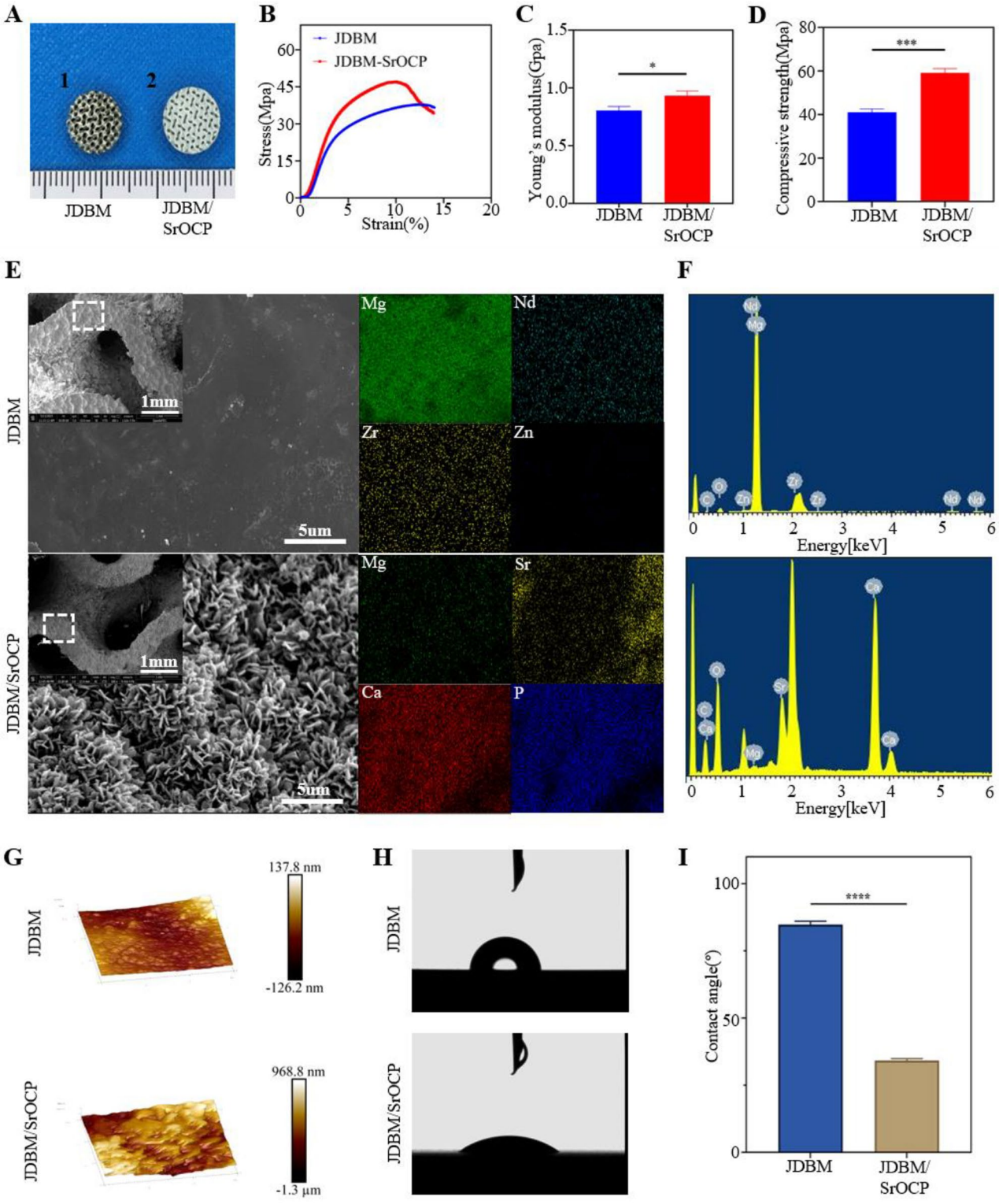

Fig. 1 Characterization and surface analysis of the scaffolds. (**A**) Representative photographs of scaffolds. (**B**) Stress-strain curves of JDBM scaffold and JDBM/SrOCP scaffold. (**C**) Young's modulus. (**D**) Compressive strength. (**E**) Surface morphology and elemental distribution of JDBM scaffolds and JDBM/SrOCP scaffolds examined by SEM and EDS. (**F**) different element contents on the surface of JDBM scaffolds and JDBM/SrOCP scaffolds examined by EDS. (**G**) Surface micromorphology of JDBM scaffolds and JDBM/SrOCP scaffolds examined by AFM. (**H**) water contact angle and (**I**) statistically analyzed.*n*=3. [<0.05 (*), <0.001 (***), <0.0001 (****)]

Table 1 Macropore size, porosity and connectivity of scaffolds

Group($n=3$)	JDBM	JDBM/SrOCP	CAD model
Macropore size(um)	728.57 ± 12.64	666.39 ± 13.39	710
Porosity(%)	72.08 ± 1.26	65.58 ± 1.69	69.73
Connectivity (%)	100	100	100

findings confirm the excellent corrosion resistance of the JDBM/SrOCP scaffold.

In vitro biocompatibility of biomimetic scaffolds

Figure 3 shows the results of biocompatibility experiments. Scaffold extracts were prepared following international standards and co-cultured with HBMSCs and HUVECs, respectively. On the seventh day, live and dead staining revealed a significant number of viable cells (both HBMSCs and HUVECs) in all three different culture environments (Fig. 3A, B). Notably, the JDBM/SrOCP group exhibited a remarkably lower number of dead cells than the blank group. However, the number of dead cells (both HBMSCs and HUVECs) was higher in the JDBM group. The viability of HBMSCs and HUVECs was further assessed using the CCK-8 assay (Fig. 3C, D). The HBMSC viability test revealed that the JDBM/SrOCP group significantly promoted HBMSC growth compared to the blank group (Fig. 3C). On the first day, the proliferation of HBMSC in the JDBM group was slightly inhibited but it subsequently increased. The HUVEC viability assay indicated (Fig. 3D) that compared to the blank group, the JDBM/SrOCP group did not exert a significant pro-proliferative effect on HUVECs on the first day, but later demonstrated a significant pro-proliferative effect in the subsequent days. On the other hand, the intervention of the JDBM group in HUVECs seemed to slightly inhibit proliferation. Furthermore, the Ki67 cell proliferation assay results revealed (Fig. S1-S2, Supporting Information 2) that compared to the blank group, the population of both cell groups in a proliferative state after the intervention of the JDBM and JDBM/SrOCP groups was significantly higher, with the JDBM/SrOCP group showing the highest number of cells.

Herein, HBMSCs were co-cultured with different scaffolds through indirect contact for the immunofluorescent detection of Vinculin expression (Fig. S3, Supporting Information 2). Compared to the control group, both the JDBM and JDBM/SrOCP groups exhibited significantly higher adhesion plaque expressions, with the JDBM/SrOCP group showing the highest expression. The focal adhesion protein was primarily localized in the cytoplasm distal to the nucleus, whereas in the control and JDBM groups, it was mainly localized in the cytoplasm proximal to the nucleus. The morphological features of HBMSCs on the surface of the JDBM/SrOCP scaffold were further examined using SEM. According to the results (Fig. 3E), HBMSCs adhered to and spread across the scaffold's surface, showing cellular proliferation states characterized by elongation and filamentous extensions. These findings confirm the excellent biocompatibility of the JDBM/SrOCP scaffold.

In Vitro osteogenic properties of biomimetic scaffolds

The osteogenic effect of JDBM/SrOCP scaffolds was assessed through alkaline phosphatase and alizarin red staining. Alkaline Phosphatase (ALP) is an early marker of HBMSC osteogenic differentiation. The ALP results (Fig. 4A, B) were observed after co-culturing two groups of HBMSCs with extracts from JDBM and JDBM/SrOCP scaffolds and subjecting them to osteogenic induction for 7 and 14 days, respectively. All groups exhibited positive staining at the predetermined time points, with the JDBM/SrOCP group showing the most intense staining throughout the experiment. Furthermore, the most intense staining was observed on day 14, and the control group showed the weakest staining intensity across all time points. Mineral deposition is a crucial foundation for new bone formation. After co-cultivation of HBMSCs with extracts from JDBM and JDBM/SrOCP scaffolds, along with osteogenic induction for 21 days, alizarin red S staining revealed (Fig. 4C) that the JDBM/SrOCP group had the highest number of calcium nodules, followed by the JDBM group.

Real-time Polymerase Chain Reaction (Rt-PCR) and IF staining were used to assess the expression of crucial target genes and proteins during the JDBM/SrOCP scaffold-induced HBMSC osteogenic differentiation. Given that the osteogenesis process is time-dependent, we co-cultured HBMSCs with osteogenic extracts from JDBM and JDBM/SrOCP scaffolds to examine osteogenic genes and proteins on days 7 and 14, respectively. The RT-PCR results demonstrated that compared to the JDBM group, the expression of early osteogenic genes (ALP, COL1, and Runx2) was significantly higher in the JDBM/SrOCP group after seven days of Conditioned Medium (CM) culture (Fig. 4D-F). Moreover, both groups showed higher expression levels compared to the blank group. These results (Fig. 4H, Figs. S4-S5, Supporting Information 2) were consistent with IF staining for corresponding osteogenic proteins (COL1 and Runx2). After 14 days of co-culture, RT-PCR and IF analysis revealed (Fig. 4G, H-L, Figs. S6-S7, Supporting Information 2) the upregulation of the late osteogenic marker gene (OCN) and osteogenic proteins (OCN and OPN). These findings confirmed the favorable osteogenic properties of JDBM/SrOCP scaffolds.

Effects of biomimetic scaffolds on HUVEC migration and angiogenesis

The cancellous bone is highly vascularized, and rapid neovascularization is required for efficient bone defect

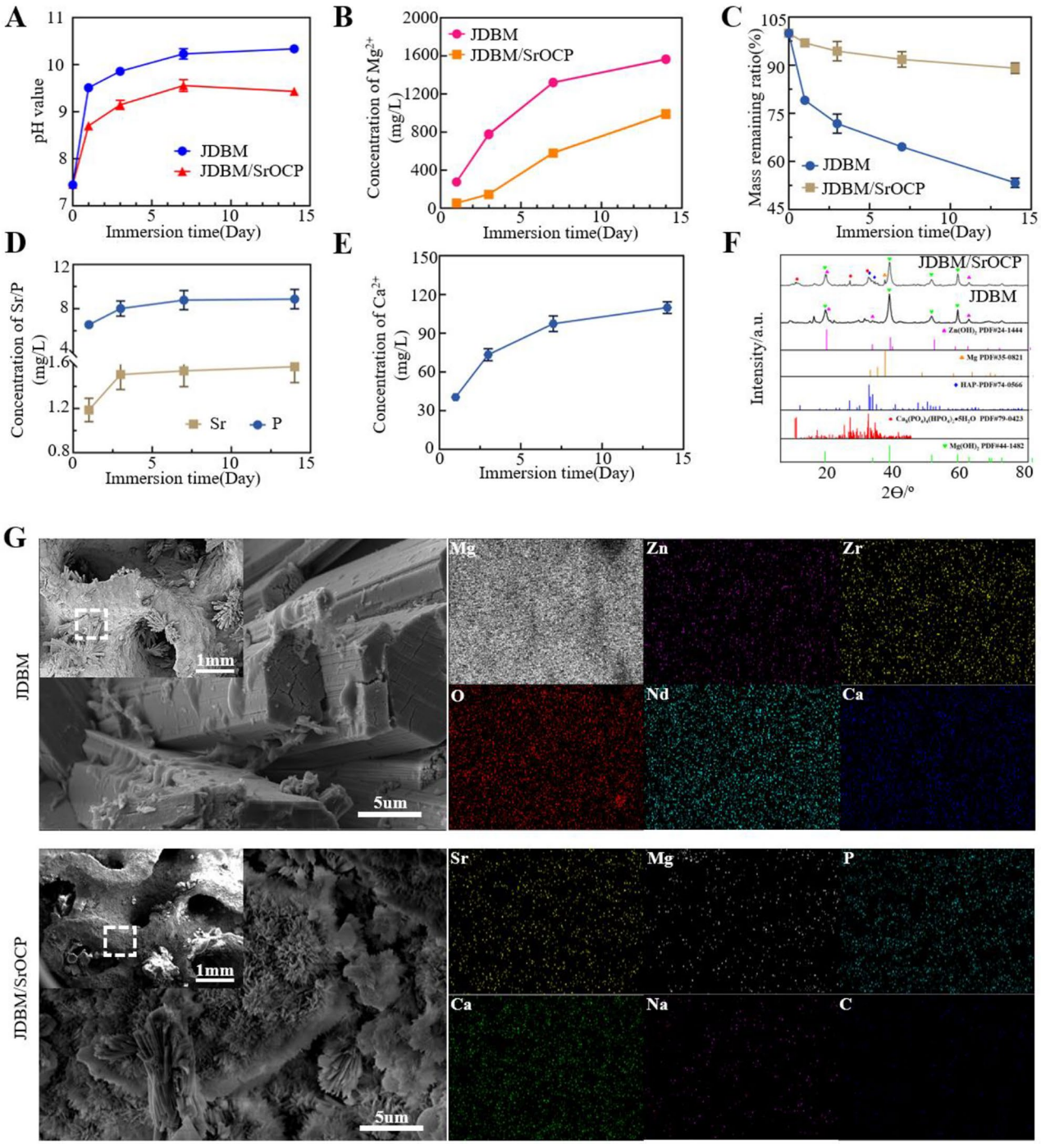

Fig. 2 Degradation behavior of JDBM scaffolds and JDBM/SrOCP scaffolds in vitro. Extracts of JDBM scaffolds and JDBM/SrOCP scaffolds were collected after 1, 4, 7, and 14 days of immersion in Hank's solution. (**A**) PH of the scaffolds extract. (**B**) Concentration of Mg2+ ions after soaking JDBM and JDBM/SrOCP scaffolds in Hank's solution for 1, 4, 7, and 14 days. (**C**) the corresponding mass changes of these membranes in vitro. Concentration of (**D**) Sr, P ions and (**E**) Ca ions after soaking JDBM/SrOCP scaffolds in Hank's solution for 14, 7, and 14 days. (**F**) XRD pattern. (**G**) SEM and (**H**) EDS scan of samples after 7-days immersion in Hank's solution

repair. Therefore, scaffold implantation-induced vascularization is crucial for bone regeneration. The HUVEC migratory capacity was evaluated through scratch and Transwell assays following in vitro co-culture with extracts derived from JDBM and JDBM/SrOCP scaffolds. According to the scratch experiment results (Fig. 5A, B), the JDBM/SrOCP group had a higher healing rate than the JDBM and blank groups, with the blank group having

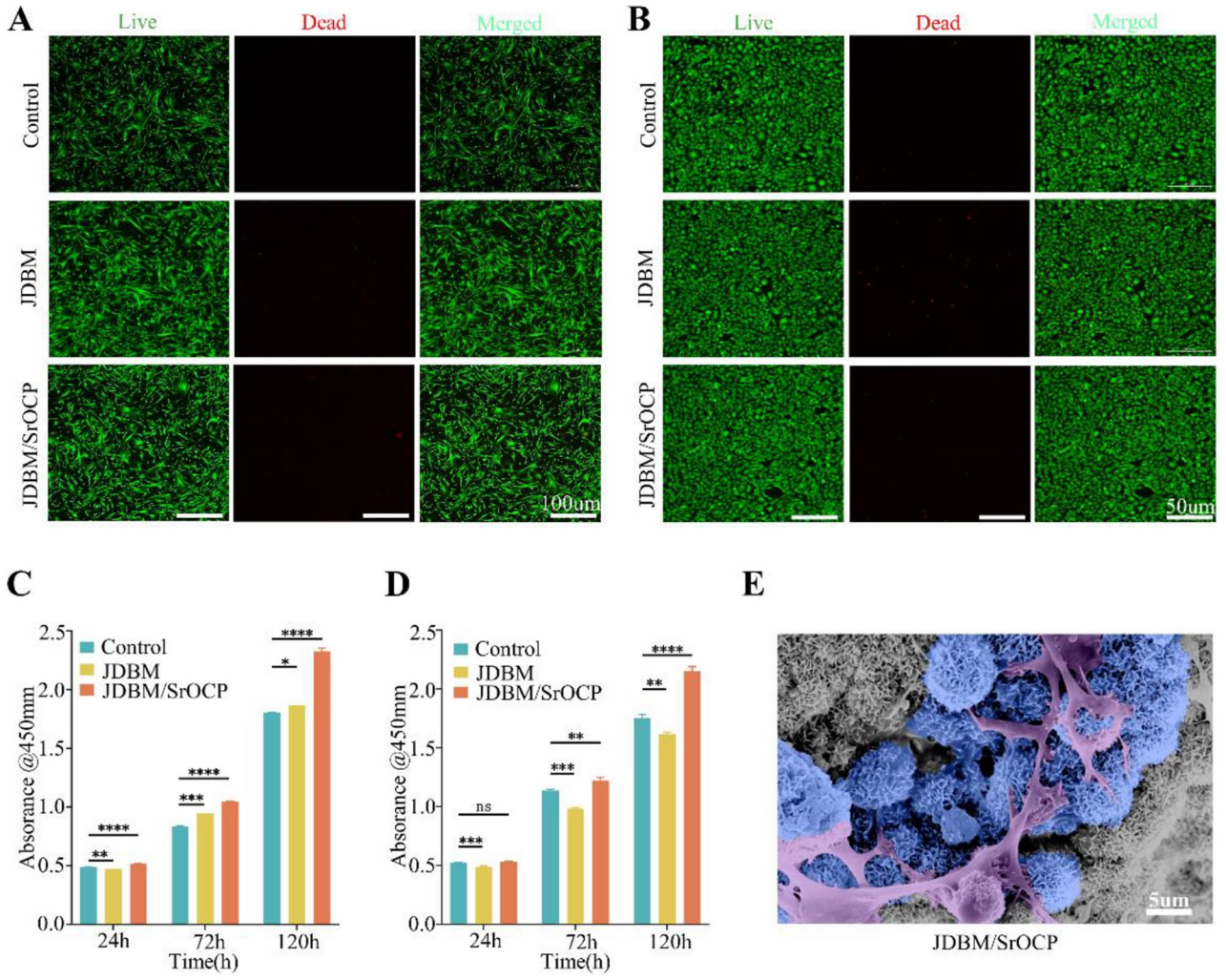

Fig. 3 Biocompatibility assessment. (**A**) Live/dead cell staining of HBMSCs. The red cells represent dead cells and the green represent live cells. (**B**) Live/dead cell staining of HUVEC. The red cells represent dead cells and the green represent live cells. (**C, D**) Cell proliferation values of HBMSCs and HUVEC obtained using the Counting Kit 8 on days 1, 3,5 in each group. (**E**) Attachment of HBMSCs to JDBM/SrOCP scaffolds observed by SEM. [<0.05 (*), <0.01 (**), <0.001 (***), <0.0001 (****)]

the lowest healing rate. The Transwell experiment results (Fig. 5C, D), on the other hand, showed that the number of migrated HUVECs was highest in the JDBM/SrOCP group and lowest in the blank group.

The impact of the JDBM/SrOCP scaffold on HUVEC vascularization in vitro was assessed using the tube formation assay. According to the results (Fig. 5E), HUVECs treated with the extract from the JDBM/SrOCP scaffold exhibited distinct and uninterrupted tubular structures within 6 h, whereas those treated with extracts from either the JDBM group or blank group showed fragmented tubular structures within the same period. The total tubule length and the number of nodes and junctions were quantified using ImageJ software. The results demonstrated (Fig. 5F-H) that all angiogenesis parameters were significantly higher in the JDBM/SrOCP group than in both the JDBM and blank control groups. Notably, the blank control group exhibited the lowest values for these parameters. Furthermore, the expressions of angiogenesis-related genes (CD31 and VEGF) were detected using RT-PCR. The results showed that the JDBM/SrOCP group significantly upregulated the transcriptional levels of CD31 and VEGF (Fig. 5I, J). These findings confirmed the enhanced angiogenic potential of the JDBM/SrOCP scaffolds.

The mechanism underlying the osteogenic and angiogenic properties of JDBM/SrOCP scaffolds

The findings of our previous study confirmed the osteogenic and angiogenic properties of JDBM/SrOCP scaffolds. However, to further explore the mechanisms underlying their biological functions, we sequenced the transcriptome of scaffold extracts after co-culturing with HBMSCs. The heatmap illustrates the expression

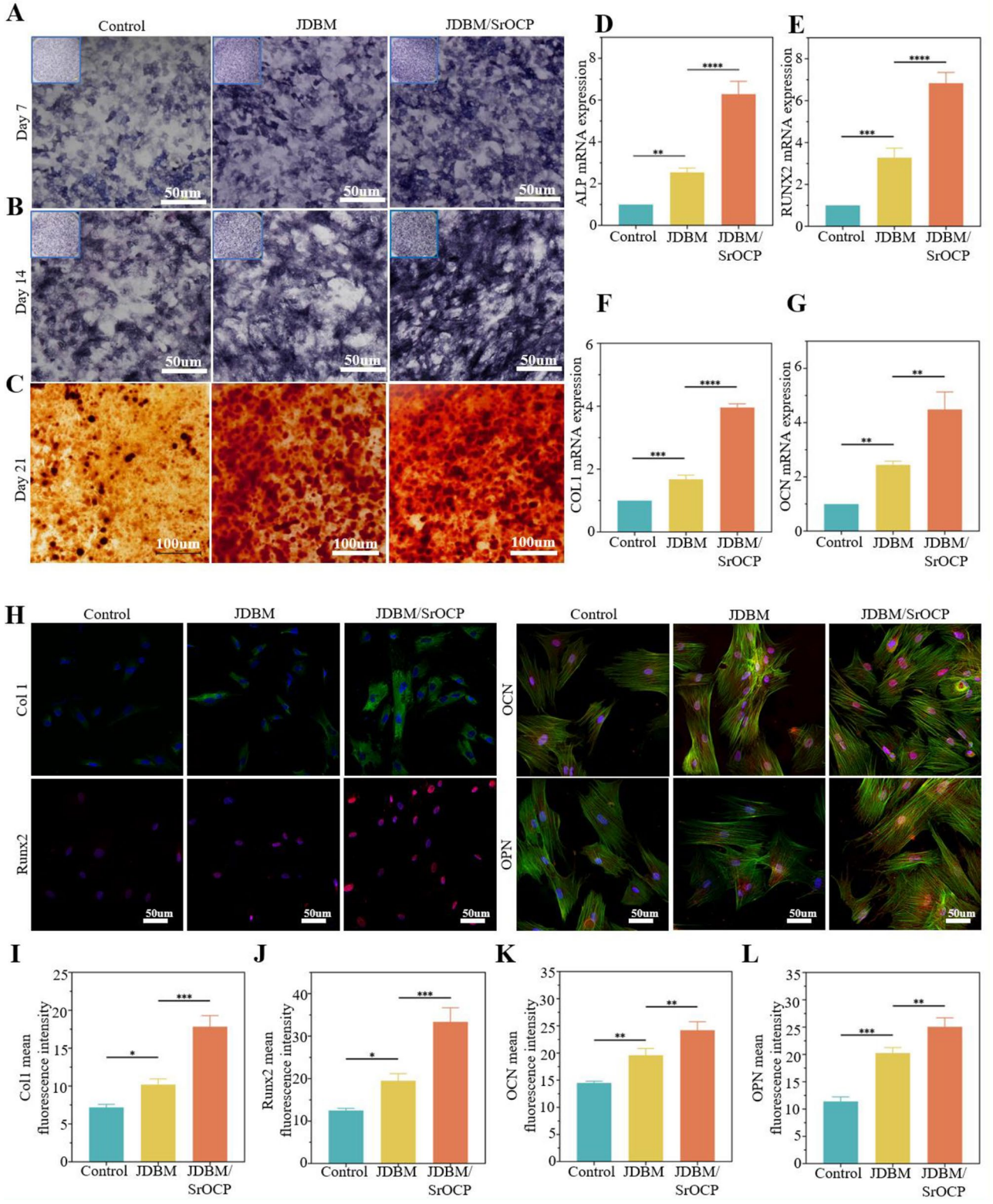

Fig. 4 In vitro osteogenic differentiation properties. (**A**) Alkaline phosphatase staining following 7 days of co-culture with HBMSCs. Scale bar: 50 μm. (**B**) Alkaline phosphatase staining following 14 days of co-culture with HBMSCs. Scale bar: 50 μm. (**C**) alizarin red staining following 21 days of co-culture with HBMSCs. Scale bar: 100 μm. (**D-G**) RT-PCR to showed relevant mRNA expression. These genes included ALP, Runx2, Col-1, and OCN. (**H**) The effects of scaffolds on the expression of Col1 (green), Runx2 (red), OCN (red) and OPN (red) at 7 and 14 days. Green shows the skeleton.The nucleus was counterstained with DAPI (blue). (**I-L**) Quantification of immunofluorescence intensity. [<0.05 (*), <0.01 (**), <0.001 (***), <0.0001 (****)]

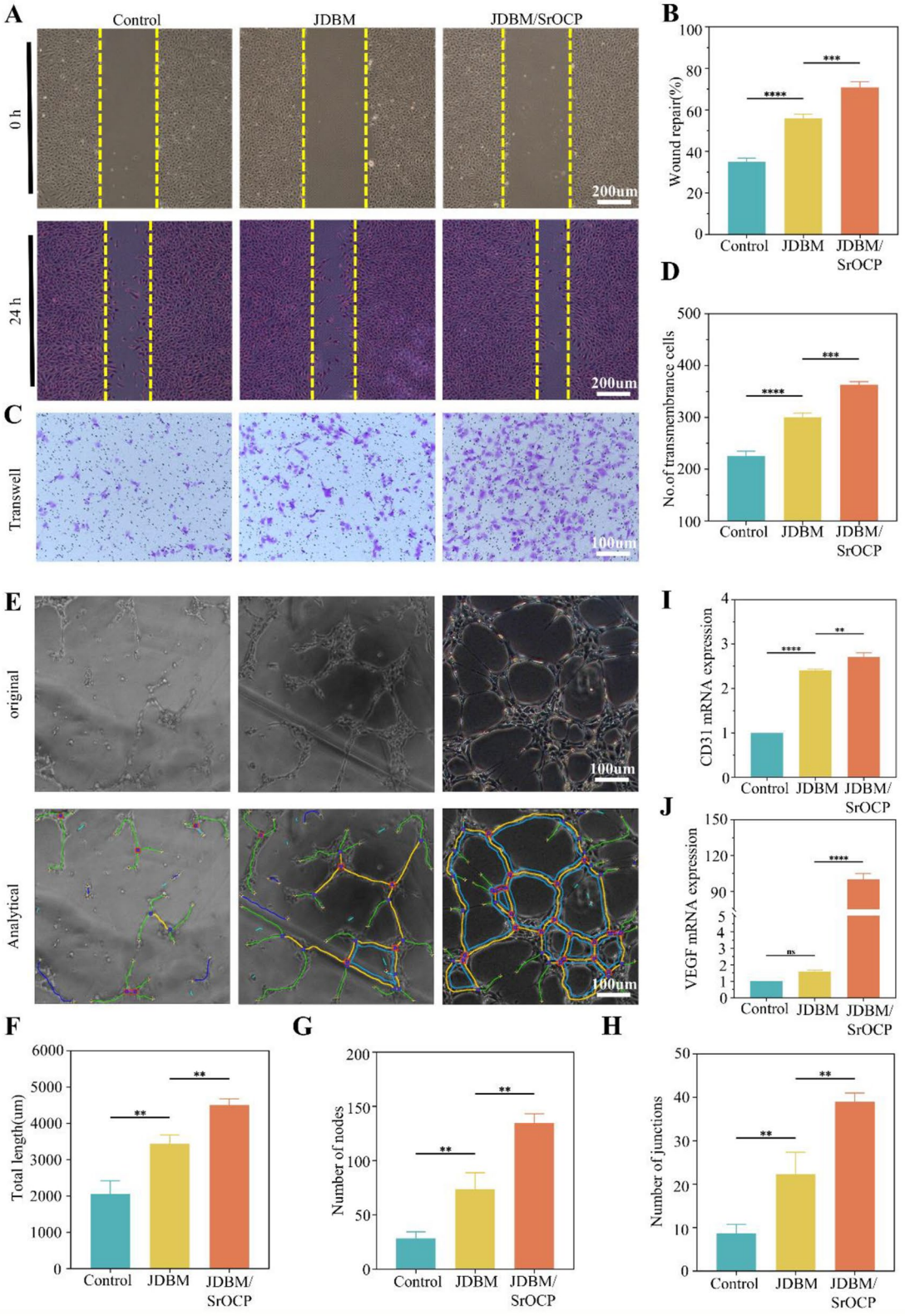

Fig. 5 Effect of different scaffolds on HUVECs migration and angiogenesis. (**A**) Representative images of scratch wound healing assay at 0 and 24 h (scale bar = 200 μm). (**B**) Statistical analysis of wound healing. (**C**) Representative images of the transwell migration assay at 24 h (scale bar = 100 μm). (**D**) Quantitative analysis of migrated HUVECs. (**E**) The tubular network formation of HUVECs after 6 h incubation (scale bar = 100 μm). (**F-H**) Analysis of difference in total length (**F**), number of nodes (**G**) and junctions (**H**) between groups. (**I, J**) RT-PCR to showed relevant mRNA expression. These genes included CD31 and VEGF. [<0.01 (**), <0.001 (***), <0.0001 (****)]

patterns of differentially expressed genes (DEGs) in HBMSCs, with red and blue indicating upregulated and downregulated genes, respectively (Fig. 6A). Specifically, 641 DEGs (P value < 0.05 &|log2 Fold Change| > 1) were identified, of which 448 and 193 were upregulated (red) and downregulated (green), respectively (Fig. 6B). The DEGs were annotated using the Gene Ontology (GO) database (Fig. 6C), and their main focus was on promoting cellular adhesion, proliferation, and migration. These genes were found to regulate various cell developmental mechanisms, molecular functions, vascular regeneration, and angiogenesis. Enrichment analysis of DEGs was performed using the Kyoto Encyclopedia of Genes and Genomes (KEGG) database (Fig. 6D) to explore the potential signaling pathways implicated in osteogenesis and angiogenesis. The DEGs were upregulated in PI3K-Akt, cAMP, cell adhesion, Extracellular Matrix (ECM)-receptor interaction, Mitogen-Activated Protein Kinase (MAPK), and Wnt signaling pathways. The GO and KEGG analyses revealed that JDBM/SrOCP scaffolds could remarkably enhance cell adhesion and signaling, guide the formation of vascular systems, and promote vascular and bone regeneration potential.

In vivo osteogenic and angiogenic properties of the JDBM/SrOCP Scaffold

Based on the results of in vitro experiments, a rat femoral condylar bone defect model was constructed and used to further verify the bionic scaffold's in vivo vascularization and osteogenic properties. The model was created by drilling a cylindrical defect with a diameter of 2.6 mm and a depth of 2.8 mm into the right medial femoral condyle of rats. The animals were then divided into blank, JDBM, and JDBM/SrOCP groups and scanned with micro-CT at 4, 8, and 12 weeks. Micro-CT results (Fig. 7A, B) revealed new bone formation in all three groups at 4 weeks post-surgery. However, the blank group exhibited less new bone formation, primarily at the defect periphery, whereas the JDBM and JDBM/SrOCP groups showed ingrowth of new bone into the

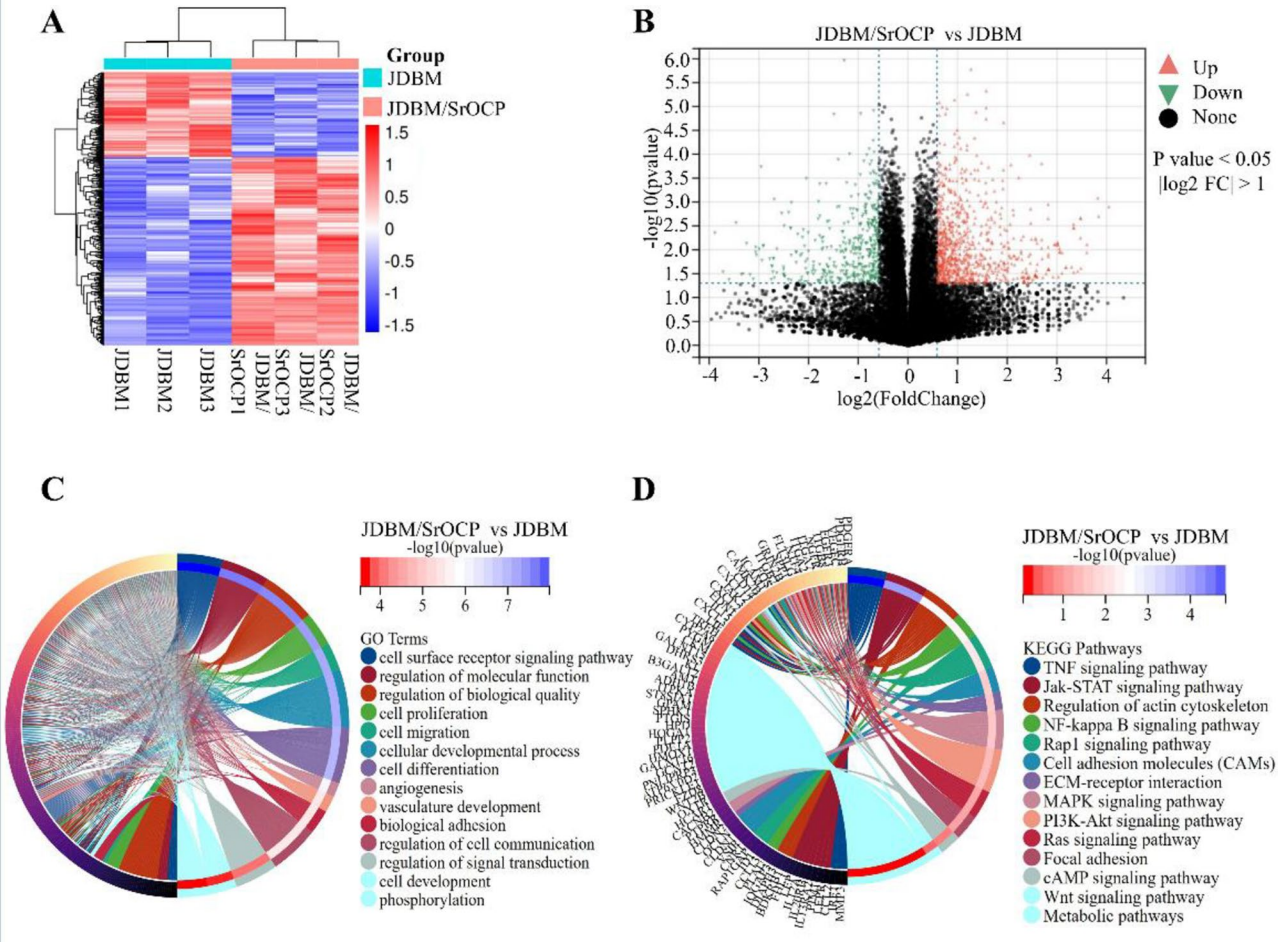

Fig. 6 Transcriptome study of HBMSCs. (**A, B**) Significantly differentially expressed genes identified by transcriptome sequencing are shown in the heatmap and volcano plot, the activated genes are marked in red and the silenced genes are marked in green (blue). Cutoff: P value < 0.05 and|log2 FC| > 1. (**C**) Circos plots depict of GO enrichment analysis. (**D**) Circos plots depict of KEGG enrichment analysis

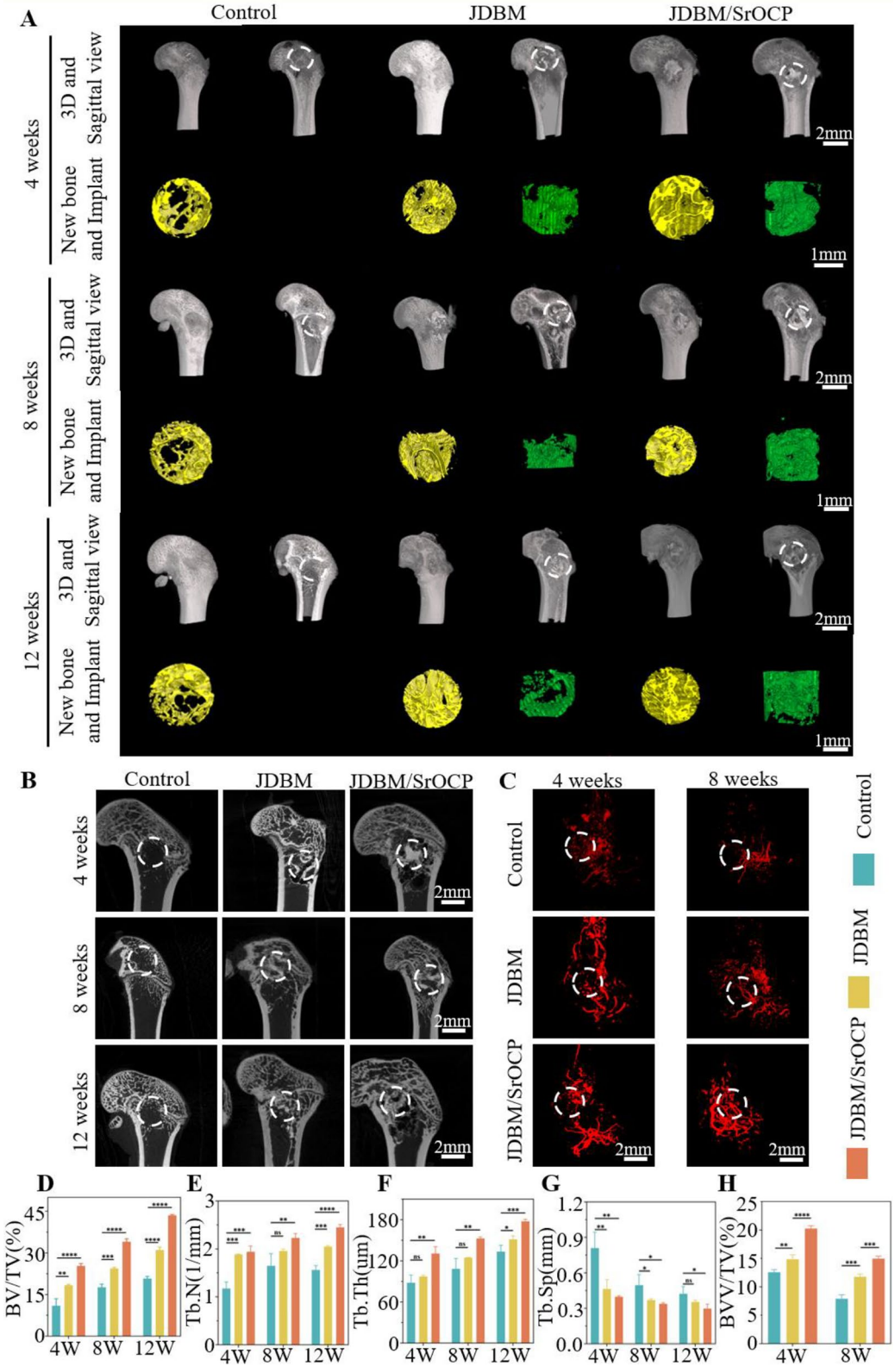

Fig. 7 Micro CT analysis of osteogenesis and angiogenesis in vivo. (**A, B**) Micro-CT images at 4, 8, and 12 weeks of in vivo implantation including new bone (yellow) and implants (green) images. (**D-G**) Quantitative analysis of osteogenic ability. (**C**) 3D reconstructed images of the internal vessels detected by micro-CT in scaffolds at 4, 8 weeks after implantation. (**H**) Quantitative analysis of the vessel volume. [<0.05 (*), <0.01 (**), <0.001 (***), <0.0001 (****)]

defect area. Further increases in new bone formation were noted in all three groups at 8 and 12 weeks post-operation, with the JDBM/SrOCP group showing the highest amount. Conversely, the blank group showed minimal new bone formation within the defect area, and the little that was observed remained concentrated at the edges. New bone formation was accompanied by scaffold degradation. Micro-CT reconstruction of the scaffold revealed (green) that at week 4, the JDBM group showed localized disintegration and small internal degradation of its scaffolds, and at weeks 8 and 12, its scaffold structure disintegrated, with the cavities inside the scaffolds and the scaffold morphology disappearing. In contrast, only a localized degradation of the scaffolds was observed in the JDBM/SrOCP group at the aforementioned times, with the bulk of the structure remaining intact. Based on the Micro-CT results observed at the sagittal position (Fig. 7B), the blank group still showed defective areas at all three time points, while the JDBM group had localized vacant areas due to the faster rate of scaffold degradation, implying that the rate of neoblastic bone generation was lower than the rate of scaffold degradation. On the other hand, the JDBM/SrOCP group had a slower scaffold degradation rate with a large number of neoblastic bone signals distributed in the degradation area. These findings indicated that the scaffold had a degradation rate closely matching the new bone generation rate. Micro-CT analysis parameters (Fig. 7D-G) revealed that the JDBM/SrOCP group exhibited significantly higher BV/TV, Tb.N, and Tb.Th levels compared to the other two groups at all three time points, while an opposite trend was observed for Tb.Sp. Bone mineral density (BMD) results exhibited a similar trend 12 weeks following scaffold implantation (Fig. S11, Supporting Information 2).These findings demonstrate superior tissue integration and an accelerated new bone formation rate in the JDBM/SrOCP group.

The regeneration rate and early neovascularization are crucial foundations for bone regeneration. A cylindrical defect with a diameter of 2.6 mm and a depth of 2.8 mm was drilled into the right medial femoral condyle of rats. Herein, regeneration rate and early neovascularization parameters were examined using the rat femoral condylar bone defect model. The animals were divided into the blank, JDBM, and JDBM/SrOCP groups, and then the samples were collected at 4 and 8 weeks post-surgery, followed by a decalcification-assisted Micro-CT scanning. According to the results (Fig. 7C, H), all groups showed neovascularization at 4 weeks post-stent implantation, with the JDBM/SrOCP group exhibiting the highest number of neovascularizations. However, at this time point, neovascularization in all three groups was primarily intermittent and displayed branching characteristics. At 8 weeks post-implantation, the number of new blood vessels decreased to varying extents compared to at 4 weeks. Nevertheless, the JDBM/SrOCP group exhibited the highest number of new blood vessels, while the blank group showed the lowest. Blood vessels also appeared mature and continuous at this stage. These findings indicate that JDBM/SrOCP scaffolds can promote early neovascularization and direct vascular ingrowth into the scaffold, facilitating sufficient nourishment in the bone defect area during the initial stage.

Histological evaluation

Figure 8A presents the results of the histological evaluation of undecalcified hard tissue sections, with orange-red and green representing newly formed and mineralized bones, respectively. Over time, the number of new bones progressively increased in all three groups, with the JDBM/SrOCP group having the highest number, followed by the JDBM group. The blank group exhibited the fewest number of new bones, primarily localized at the periphery of the defect area, with minimal new bone formation within the defect region. The JDBM and JDBM/SrOCP scaffolds demonstrated excellent integration with newly formed bones, showing favorable osseointegration. Before implantation, JDBM scaffolds exhibited rapid degradation at 4 weeks, characterized by cavities in the defect area. Only a small portion of the scaffolds remained at 8 weeks, and the cavity size was partially reduced. Furthermore, at 12 weeks, JDBM scaffolds were essentially degraded, with some residual cavities still present. Conversely, JDBM/SrOCP scaffolds showed a slower degradation rate. After 4 weeks of implantation, the scaffold only showed a localized degradation while its main structure remained intact and filled with newly formed bone tissues. At 8 weeks, further degradation occurred in the scaffold's outer layer, but its core structure was maintained, promoting new bone formation. Additionally, at 12 weeks post-implantation, the inner layer of the scaffold began to degrade and was accompanied by the filling of the inner neoplastic bone tissue, but without obvious cavity formation. Overall, the JDBM/SrOCP scaffold showed superior osseointegration and significantly enhanced the ingrowth of new bone compared to the JDBM scaffold.

The scaffolds' early vascularization and bone regeneration abilities were further assessed using paraffin Sections 4 weeks post-implantation. The HE and Masson staining results were consistent with those observed in hard tissue sections (Fig. 8B, C). Moreover, based on HE staining, there were no apparent signs of inflammatory reactions or necrosis across all groups. Examination of vital organs in rats using HE staining also revealed no apparent inflammation (Figs. S8-S10, Supporting Information 2), indicating the excellent biocompatibility of all implanted scaffolds in vivo. The scaffolds' early

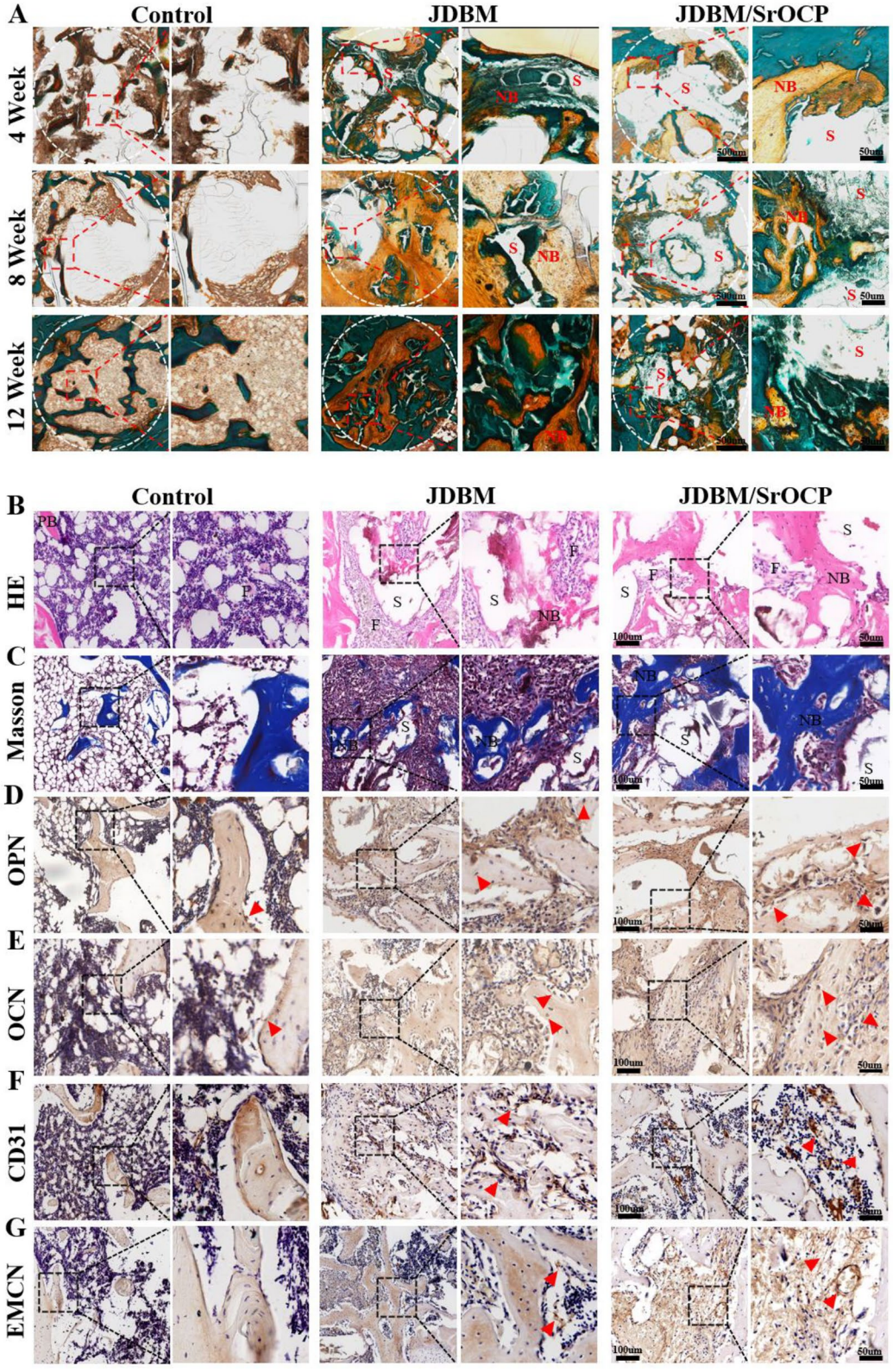

Fig. 8 Staining of tissue sections. (**A**) Full-view and enlarged images of hard-tissue slices of JDBM and JDBM/SrOCP implanted in vivo. (**B, C**) Representative pictures of HE and masson staining of bone tissue sections treated for 4 weeks in each group. (**D-G**) Representative pictures of bone tissue sections taken 4 weeks after surgery for immunohistochemical staining of OCN, OPN, CD31 and EMCN

osteogenic and angiogenesis abilities were further confirmed using Immunohistochemistry (IHC) and IF techniques. According to the IHC results (Fig. 8D, E), except for the blank group, all other groups showed significant expression of osteogenic markers (OCN and OPN) at 4 weeks. This observation corresponded to the positive expression of H-type vascular markers (CD31 and EMCN), as revealed by the IHC staining results (Fig. 8F-G). We employed IF quantification to further analyze the disparities in the expression of osteogenic and angiogenic markers across the experimental groups (Fig. 9A-F). According to the results, compared to the control group, both the JDBM and JDBM/SrOCP groups showed a significantly higher expression of bone markers (OCN and OPN), with the JDBM/SrOCP group exhibiting the highest expression. Since type H vessels are a crucial component in cancellous bone, the scaffold's angiogenic ability in vivo was assessed via IF detection of type H vessels double-labeled with CD31 and EMCN. According to the results (Fig. 9C, F), compared to the control group, both the JDBM and JDBM/SrOCP groups exhibited a significantly larger area occupied by type H vessels, with the JDBM/SrOCP group showing the greatest enhancement. These findings indicate that JDBM/SrOCP scaffolds have a high potential for vascularized bone regeneration, particularly at the early stage.

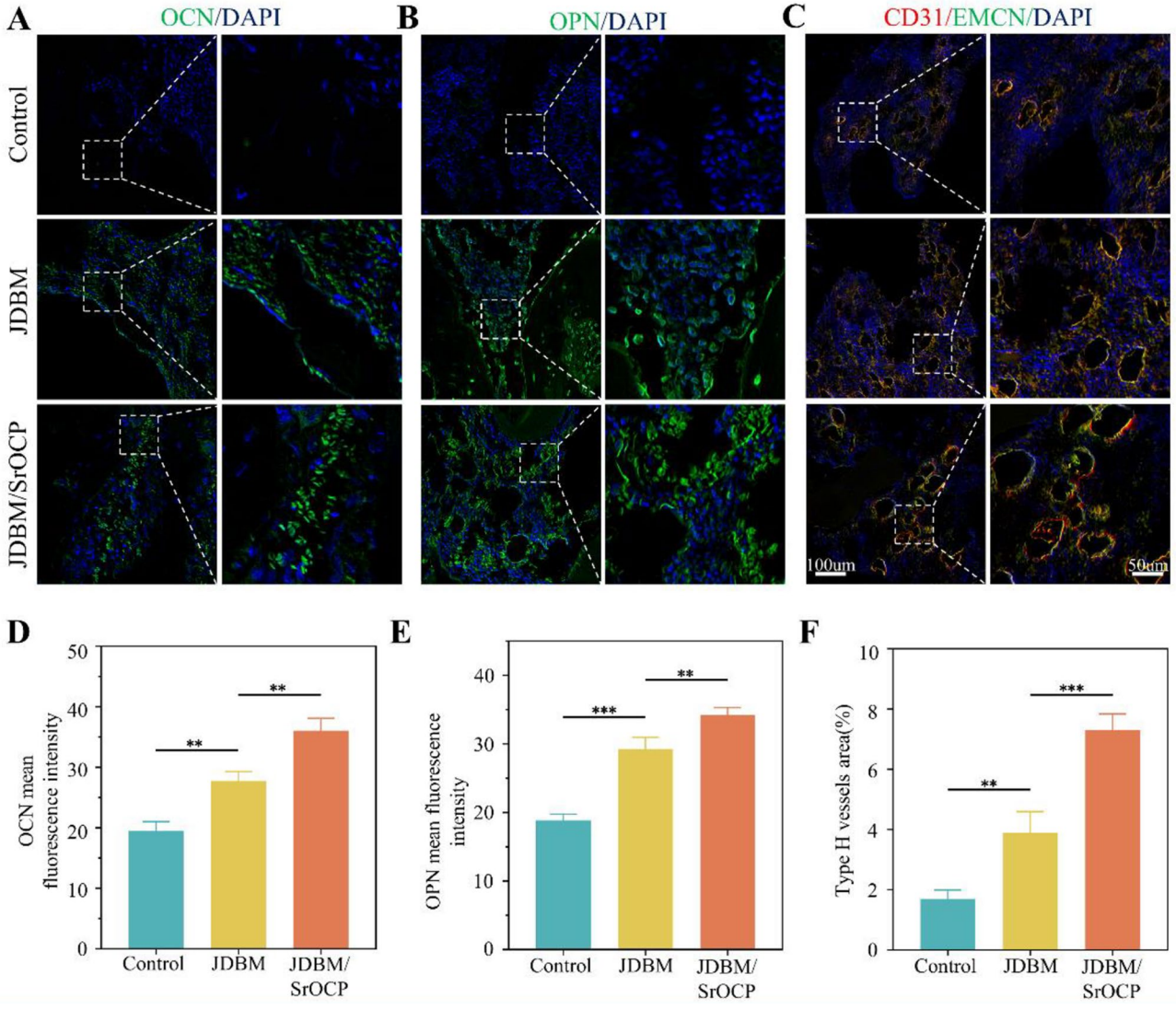

Fig. 9 Immunofluorescence staining and quantitative analysis. (**A-C**) Immunofluorescence staining of the decalcified bone slices, the osteogenesis and angiogenesis related genes OCN(green), OPN (green), CD31 (red) and EMCN (green) significantly increased in the JDBM/SrOCP group. The nucleus was stained with DAPI (blue). (**D-F**) The expression difference of related proteins was quantified. [<0.01 (**), <0.001 (***)]

Discussion

With rapid advancements in tissue engineering, biomimetics [42, 43] has presented numerous benefits in various fields and has been extensively applied in material science, biology, medicine, and other disciplines. Inspired by the unique physiological structure of sea urchins [44], we developed a biomaterial scaffold with a three-cycle minimal surface structure (TPMS) and biomimetic properties. The TPMS [45] surface is exceptionally smooth, with highly interconnected pores that facilitate cellular and tissue growth. On the other hand, the LPBF process has micron-scale precision and can replicate the intricate structure, porosity, and pore size of natural bone, facilitating the production of clinical-grade biomimetic scaffolds. Due to its favorable biosafety profile and functional properties, magnesium metal has gained significant attention in the production of clinical-grade biomimetic scaffolds. Herein, the TPMS structural scaffold was designed using Rhinoceros® 7.0 software, while the biomimetic porous magnesium alloy scaffold was fabricated using the LPBF process. Mechanical testing revealed that the porous magnesium metal scaffold had a marginally higher Young's modulus and compressive strength than cancellous bone, ensuring sufficient mechanical support for the bone defect area dring a specific degradation period.

In addition, 3D-printed hydroxyapatite, tricalcium phosphate, and other ceramic scaffolds have been extensively utilized in research related to the repair of bone defects [3]. Ceramic scaffolds possess calcium and phosphorus components similar to those of natural bone, exhibit good biocompatibility, and can provide a biomimetic microenvironment for bone defects, thereby emerging as promising materials for clinical application. Nevertheless, the mechanical properties of 3D-printed ceramic scaffolds do not fully meet the requirements for bone defects, particularly those in load-bearing areas. Moreover, the degradation rate of ceramic scaffolds is slow, and the degradation rate after implantation into the bone defect site does not align with the rate of new bone regeneration, which hinders local bone regeneration to some extent. Therefore, ceramic scaffolds need modification to fulfill the demands of clinical application. In contrast, magnesium metal can precisely regulate the porosity through 3D printing to meet the mechanical requirements of bone defects. Simultaneously, the strategy of magnesium metal surface modification can optimize the relationship between scaffold degradation and bone regeneration.

Regulating the degradation rate of magnesium alloy scaffolds ensures their efficiency in bone remodeling. Accelerated degradation could lead to the early loss of mechanical support in the bone defect area. The in vivo degradation mechanism of magnesium alloy's [46, 47] involves complex electrochemical reactions that produce $Mg(OH)_2$ and H_2 as the main byproducts.These intermediates significantly influence biocompatibility. Specifically, an optimal concentration of these intermediates could elicit favorable host responses, whereas high concentrations could disturb the local equilibrium and impact the surrounding microenvironment, affecting adjacent tissues. Therefore, the precise regulation of the magnesium alloy degradation rate directly influences the biocompatibility and biofunctionality of Mg-based implants.

Surface composite coatings are an effective strategy for preventing the early and rapid degradation of magnesium alloys. By obstructing contact between the medium and the matrix, the coatings could somewhat reduce the matrix's corrosion rate during initial implantation. Zhang et al. [47] introduced a composite DCPD coating onto the surface of 3D-printed pure magnesium porous scaffolds, achieving a reduced degradation rate of modified magnesium metal scaffolds and significantly improving biosafety. On the other hand, Yuan et al. [48] designed a DCPD coating for magnesium alloy scaffolds and compared it with the MgF_2 coating. According to the results, the DCPD coating exerted stronger protective effects on the matrix, had a slower scaffold degradation rate, and enhanced biosafety. Furthermore, Yan et al. [41] introduced DCPD and Sr-P coatings to the surface of magnesium alloy scaffolds and found that although the Sr-P coating exhibited biocompatibility comparable to the DCPD coating, it demonstrated a more favorable degradation rate and enhanced biofunctionality. Herein, we innovatively introduced strontium into the surface of a DCPD-coated magnesium alloy and hydrothermally transformed the DCPD coating into SrOCP and strontium hydrogen phosphate biphasic composite structural bioactive coatings. The composite-coated magnesium alloy scaffolds showed significantly enhanced surface roughness and hydrophilicity, offering more anchoring sites and adhesion forces for cells. These features could promote cell adhesion and facilitate crucial biological functions. Besides effectively preventing contact between the medium and the matrix, the coating also significantly lowered the release and degradation rates of the JDBM/SrOCP scaffold compared to the JDBM scaffold. These effects improved the biosafety of porous magnesium alloys by prolonging their residence time in vivo, and enabled the continuous in situ delivery of Mg^{2+}. Although this study confirmed the composite coating's protective effects on the matrix, additional research is required to precisely control the degradation behavior by adjusting for key factors such as coating thickness and bonding strength between the coating and the matrix. Additionally, an accelerated degradation time for the scaffold was not observed during the tests, indicating a possible

direction for future research on designing customized magnesium alloy scaffolds for different stages of bone defect repair.

Good biocompatibility [49] is a fundamental prerequisite in assessing the clinical translatability of biomaterials. The live and dead staining results (Fig. 3A, B) revealed that compared to the blank group, the JDBM group exhibited a higher number of dead cells. In contrast, the JDBM/SrOCP group showed a similar number of dead cells as the blank group. Based on these observations, we hypothesized that an environment high in magnesium and alkali concentrations might induce cytotoxicity in damaged cells. This speculation is consistent with previous findings [22], which posited that elevated Mg^{2+} concentrations could induce cell apoptosis. Additionally, as confirmed by the cell proliferation experiment and electron microscopy results(Fig. 3F), surface-modified porous magnesium alloy scaffolds showed improved biocompatibility, promoting cell adhesion and proliferation. This finding establishes a solid foundation for subsequent biofunctionality assessments and applications.

Bone defect restoration is attributed to the concurrent processes of new bone formation and angiogenesis [50]. These processes ensure an adequate supply of nutrients to various stem cells within the defect area, timely removal of metabolic wastes, and maintenance of the microenvironment conducive to osteogenesis. Simultaneously, in coordination with these processes, angiogenesis accelerates the bone remodeling rate, ultimately facilitating rapid repair. It is important to note that [20, 51] effective vascularized bone regeneration following magnesium metal scaffolds implantation must be established within a suitable concentration of magnesium ion environment. The rapid degradation of magnesium metal can result in the local accumulation of a large amount of magnesium ions, disrupting the microenvironment of bone homeostasis, activating osteoclasts and inhibiting endothelial cells, thereby hindering bone and vascular regeneration. Therefore, the biological function of magnesium metal scaffolds must be achieved within the context of continuous and controlled release of magnesium ions.

The effect of porous magnesium metal scaffolds on the osteogenic differentiation of mesenchymal stem cells influences the rate of bone regeneration. The process of bone defect repair using scaffolds is primarily categorized into three phases [52]: initial cell adhesion and proliferation, subsequent osteogenic differentiation, and eventual extracellular matrix mineralization.ALP, an early marker for osteogenesis [53]. and RUNX2 [54], a critical transcription factor specific to osteogenesis, modulate the maturation of osteoblasts as well as intramembranous and endochondral ossification processes. COL1 [55] is considered as a marker of osteogenic mineralization and the main component of matrix secreted by osteoblasts. OPN [56] is widely expressed in the extracellular matrix and influences the adhesion and differentiation of osteoblasts. On the other hand, OCN [57] is considered a late osteogenic marker. In this investigation, compared to the JDBM scaffold, the JDBM/SrOCP scaffold had significantly higher expression levels of early osteogenic genes such as ALP, RUNX2, and COL1, as well as late osteogenic genes like OCN. Moreover, the expression of osteogenic proteins including RUNX2, COL1, OCN, and OPN in HBMSCs was increased when compared to the JDBM scaffold.

The porous magnesium alloy scaffolds enhanced the migration ability and tubule formation of HUVECs [58]. In this study, we investigated the impact of scaffold surface modification on HUVEC migration using scratch and Transwell assays. It was observed that incorporating JDBM/SrOCP into the scaffold significantly enhanced HUVEC migration relative to the JDBM scaffolds. The ability of HUVEC to form tubes in vitro was demonstrated in this experiment. The results indicated that the JDBM/SrOCP scaffold exhibited superior vascular parameters. Guo et al. [17] found that porous polyetheretherketone (PEEK) surfaces, printed in 3D and coated with magnesium, promoted the migration and tube formation of HUVECs. Similarly, Wang et al. [59] reported a significant improvement in HUVEC migration and tube formation capacity following the application of composite magnesium coating on hydroxyapatite surfaces. The transcription factors CD31 and VEGF regulate angiogenesis. In this study, the JDBM/SrOCP scaffold significantly upregulated CD31 and VEGF gene expression, as confirmed by RT-PCR analysis. Therefore, we suggest that JDBM/SrOCP scaffolds augment the recruitment, migration, and tube formation capabilities of HUVEC cells, which is consistent with previous findings [60].

Transcriptomic analyses revealed that the differentially expressed genes were mainly strongly associated with cellular adhesion, proliferation, and migration, as well as the regulation of crucial cell developmental processes and molecular functions. Therefore, we postulated that the JDBM/SrOCP scaffolds enhance cellular proliferation and differentiation by recruiting cells and providing adhesive sites for cellular attachment. Simultaneously, the expression of genes associated with tissue regeneration, such as angiogenesis, blood vessel formation, and bone regeneration, was significantly upregulated. The crucial signaling pathways including PI3K-Akt, cAMP, cell adhesion, ECM-receptor interaction, mitogen-activated protein kinase (MAPK), and Wnt were observed to be up-regulated. This indicates their potential dominance in angiogenesis and bone regeneration, offering valuable insights for our forthcoming mechanism investigations.

Together with the in vitro results, JDBM/SrOCP scaffolds were implanted into the SD rat femoral condyle defect model to investigate the bone formation effect in vivo. The growth of new bone in the bone defect area was analyzed using Micro-CT and non-decalcified hard tissue sections. In the control group, bone regeneration was restricted to the edges of the bone defect area as there was no scaffold support, and its growth pattern proceeded from the periphery towards the center. In contrast, in both the JDBM group and JDBM/SrOCP group, porous scaffolds allowed infiltration of various regenerative cells into their pores, promoting close adhesion and enabling corresponding biological functions. As a result, the introduction of scaffolds disrupted traditional bone healing processes, leading to an inside-out healing mechanism and hastened bone regeneration. During the initial stage of implantation, the JDBM scaffold showed rapid degradation. After 4 weeks, corrosion was noted at the periphery, along with localized internal degradation. At 8 weeks and 12 weeks post-implantation, the scaffold had completely disappeared, leading to a loss of mechanical support within the bone defect area. The JDBM/SrOCP scaffolds exhibited a gradual and uniform degradation pattern, with only slight corrosion observed after 4 weeks of implantation. The corroded area was rapidly replaced by new bone tissue. After 8 weeks and 12 weeks of implantation, the periphery of the scaffold degraded while the inner region was gradually replaced by new bone tissue. However, the primary structure of the scaffold remained intact thereby providing mechanical support for bone defect areas. These findings suggest that JDBM/SrOCP scaffolds possess excellent osseointegration, osteoconductivity, and osteoinduction properties and their degradation rate is matches the growth rate of the new bone. Further research is advocated to address the degradation rate of scaffolds and changes in their mechanical properties after implantation in bone defect areas. This will ensure sustained mechanical support in these regions.

The rate of neovascularization in the bone defect area is a key factor influencing the quality of bone regeneration [61]. Adequate and timely vascularization in the area of bone defect can ensure ample nutrient supply and abundant oxygen provision to the local region, while also facilitating the continuous influx of osteoprogenitor cells and other essential elements.In this study, microvascular imaging was conducted to analyze early angiogenesis within the bone defect region. Micro-CT was employed to assess the initial neovascularization regeneration. The findings revealed a significant increase in neovascularization in all groups 4 weeks post-stent implantation. However, at this stage, the neovascularization exhibited disorganized, discontinuous, and branched patterns, suggesting an immature state. By the eighth week of scaffold implantation, neovascularization was reduced in all groups. Nevertheless, the blood vessels exhibited high completeness, continuity, and maturity. CD31 and EMCN are potential markers for type H vessels, a specialized blood vessel subtype in bone that facilitates angiogenesis and new bone regeneration. Immunofluorescence quantitative analysis further demonstrated a significant increase in the positive area of CD31 and EMCN in both groups, with the JDBM/SrOCP scaffold group exhibiting the largest positive area. The immunohistochemical and immunofluorescence results of OCN and OPN at 4 weeks after scaffold implantation were similar to those of type H vessels, indicating that the JDBM/SrOCP scaffold could effectively promote early vascularized bone regeneration in the bone defect area. This observation was further supported by results of the ion release curve and tube formation obtained in vitro.

Following a bone defect, various cells converge to create a local intricate microenvironment, pivotal in the repair process. Research suggests [62] that the introduction of bone materials during implantation can modulate biological functions by affecting this local microenvironment. Studies have demonstrated [63] that appropriate concentration of magnesium ions can activate osteogenic and angiogenic microenvironments, thereby enhancing new bone formation. In summary, we conclude that JDBM/SrOCP scaffold dominates the local microenvironment by enabling a sustained release of Mg ions, consequently promoting early vascularization and long-term bone regeneration within the area affected by bone defects.

In summary, we fabricated a biomimetic, structure porous magnesium alloy scaffold through 3D printing. The mechanical properties of the scaffold were similar to those of natural bone. Furthermore, a hydrothermal conversion method was employed to coat the scaffold's surface with nano-bioactive coatings, effectively regulating its degradation rate and enabling controlled release of magnesium ions. Although the viability and biological efficacy of the JDBM/SrOCP scaffold were thoroughly assessed, further studies should aim to investigate the spatial dimension degradation behavior of magnesium metal scaffolds to fulfill the demands of bone repair. In addition, it is important to modulate the mechanical changes associated with the degradation process of magnesium metal in vivo to properly repair defect areas. This can be achieved by investigating structural and coating modifications for magnesium alloys. Moreover, further studies using large animals and specific pathological models are needed to uncover the metabolic mechanisms and immune regulation pathways related to magnesium ions in vivo, to promote the clinical translation of porous magnesium alloy scaffolds.

Conclusions

In this study, we successfully fabricated nano-bioactive coatings on the surface of JDBM scaffolds via hydrothermal transformation to achieve controlled and rapid degradation of the scaffolds. The controlled release of magnesium ions potentiated the effect of JDBM/SrOCP scaffolds on promoting angiogenesis and osteogenesis abilities. In comparison to the JDBM scaffold, the JDBM/SrOCP scaffold exhibited enhanced biocompatibility and superior biological functions in vitro. These included heightened cell proliferation and adhesion, facilitated osteogenic differentiation of HBMSCs, and induced tube formation in HUVEC cells. In vivo assessments through Micro-CT imaging and histological examination demonstrated that the JDBM/SrOCP scaffolds effectively facilitated early blood vessel formation and ingrowth into the scaffold, thereby expediting the bone regeneration process. In conclusion, JDBM/SrOCP scaffolds have excellent osseointegration, osteoconductivity, and osteoinductivity. This study provides a novel strategy for the clinical management of bone defects.

Experimental section

Scaffold preparation

3D model design

The Rhinoceros® 7.0 modeling software and its parametric modeling plug-in Grasshopper were employed to design the support structure of the helical icosahedral Gyroid minimal surface, which was mathematically expressed through a separate formula:

$$\cos\left(\frac{2\pi}{U}x\right)\sin\left(\frac{2\pi}{U}y\right)+\cos\left(\frac{2\pi}{U}y\right)\sin\left(\frac{2\pi}{U}z\right)+\cos\left(\frac{2\pi}{U}z\right)\sin\left(\frac{2\pi}{U}x\right)=\mathrm{t}$$

Where U denotes the size of the minimum structural unit of the TPMS, t is the structural parameter that determines the shape of the minimum structural unit. Here, t = 0 is set here, the minimum structural unit size is 2 mm, the wall thickness is 0.45 mm, and the model file is saved in STL format.

Manufacturing of the scaffold

The equipment used in the laser powder bed fusion (LPBF) experiment was the ProX DMP 320 from 3D Systems. The size of the formed substrate plane was 275 mm × 275 mm × 420 mm, with the machining accuracy of the parts being ± 0.1% of the current printing range, and the oxygen content during printing was lower than 25 ppm. The LPBF parameters were as follows: laser power of 80 W, scanning speed of 400 mm/s, layer thickness of 30 μm, hatch space of 80 μm, and spot size of 80 μm. To reduce thermal stress, when scanning the adjacent layers above and below, the laser scanning direction was rotated by 73° successively. After printing was completed, the substrate and samples were taken out, and wire-electrode cutting was used to obtain the printed samples.

Table 2 Formula of DCPD treatment solution

Composition	Concentration(g/L)
$NaNO_3$	60
$Ca(H_2PO_4)_2.H_2O$	15
H_2O_2	20

Dynamic electrolytic polishing

To remove the adhesive powder on the surface of the scaffold, anhydrous ethanol solution containing 10% volume fraction perchloric acid was utilized to perform dynamic electrochemical polishing. A magnetic rotor was employed to stir at the speed of 600 rpm/min, with a polishing time of 10 min. After the polishing, anhydrous ethanol was used for ultrasonic cleaning and dried in a vacuum drying oven.

Surface fluorination treatment

The polished support was soaked in a fume hood with 40% hydrofluoric acid and shaken on a shaker for 6 h until a dense magnesium fluoride coating of about 1.5 μm thickness was formed on the surface of the scaffold. After fluorination, it was cleaned with deionized water and anhydrous ethanol.

Dicalcium phosphate dihydrate (DCPD) coating

Sodium nitrate($NaNO_3$), Calcium dihydrogen phosphate ($Ca(H_2PO_4)_2.H_2O$) purchased from Sinopharm Chemical Reagent Co., LTD., analytical pure, purity ≥ 98.0%.The porous scaffold surface was coated with DCPD using a chemical deposition method. The fluorinated scaffold was immersed in a supersaturated solution, and after 12 h of static reaction, a uniform white DCPD coating formed on the scaffold surface. The composition of the DCPD solution is detailed in Table 2 below.

5% Sr2+ octacalcium ohosphate (OCP) coating treatment

Sodium dihydrogen phosphate (NaH_2PO_4), Strontium nitrate ($Sr(NO_3)_2$), Sodium hydroxide (NaOH) purchased from Sinopharm Chemical Reagent Co., LTD., analytical pure, purity ≥ 96.0%.To improve the corrosion resistance and promote osteogenesis properties of the scaffold, a hydrothermal reaction solution containing Sr^{2+} with a molar concentration of 5% of the sum of the molar concentrations of Sr and Ca elements was prepared using a hydrothermal transformation method. The pH was adjusted to 6.5 using NaOH. The sample and solution were placed in a 500 mL hydrothermal reaction kettle. The reactor was placed in the oven to react at 90℃ for 12 h. The DCPD coating on the surface of the sample

Table 3 Chemical composition of 100mL hydrothermal reaction solution of OCP coating containing 5%Sr^{2+}

Composition	Concentration/g
NaH_2PO_4	4.90
$Sr(NO_3)_2$	0.39
Na-EDTA	0.59
Ca-EDTA	13.335
NaOH	appropriate amount

was transformed into 5Sr-OCP coating, and the appearance of the sample was gray-white matte. The formula of hydrothermal reaction liquid is shown in Table 3.

Characterization and mechanical properties of 3D printed porous scaffolds

Characterization of 3D printed scaffolds

The overall conditions of JDBM and JDBM/SrOCP scaffolds were examined using stereomicroscopy. SEM was employed to examine the scaffold surface morphology, whereas EDS was employed to observe the element distribution on the scaffold surface. The nanomorphology and surface roughness of the scaffolds were assessed using AFM analysis. The hydrophilicity of the scaffolds was determined using contact angle (CA) measurements. Porosity of the porous scaffolds was calculated using the ethanol replacement method according to the following formula [ASTM F2150–17 (2022) e1] [46]: Porosity (%)=(V_1-V_3)/(V_2-V_3) × 100%.

The volume V_1 indicates the total volume of the graduated cylinder after addition of absolute ethanol and immersion in the scaffold sample. The volume V_2 denotes the total volume recorded after removal of air from the material's pores using a vacuum desiccator and filling them with ethanol. Volume V_3 indicates the total volume of material remaining after removal from the graduated cylinder.

In vitro degradation tests

According to ASTM-G31-21, the scaffolds were immersed in 'Hank's solution (37℃, pH 7.4) at a ratio of 20 mL/cm^2. The extracts were collected on days 1, 4, 7, and 14 for analysis using ICP to measure Mg^{2+}, Sr^{2+}, Ca^{2+}, and P concentrations. Moreover, the residual weight of the magnesium metal scaffold was calculated to evaluate its degradation behavior. SEM was employed to examine the surface morphology of the scaffolds after immersion for 7 days, and EDS was utilized to observe the distribution of elements. XRD analysis was performed to determine the composition of surface products post-degradation.

Mechanical property test

The cylindrical porous magnesium scaffold support was securely positioned on the tray of the electronic universal testing machine and compressed in both the X-axis and Z-axis directions, respectively. The displacement rate was set at 1 mm/min to accurately establish the control. The load-displacement curve was automatically recorded until a displacement of 3.0 mm was reached. Finally, the stress-strain curve was plotted.

In vitro experiments

Biocompatibility of JDBM/SrOCP scaffolds

HBMSCs were collected from Wuhan Punosai whereas HUVECs were purchased from Zhejiang Meisen. HBMSCs were cultured in MSCM (complete medium supplemented with 5% fetal bovine serum, MSCGS mesenchymal stem cell growth supplement, streptomycin 100 ug/ml, penicillin 100 U/ml). HUVECs were cultured in ECM (complete medium supplemented with 5% fetal bovine serum, ECGS endothelial cell growth supplement, streptomycin 100 μg/ml, penicillin 100 U/ml). All cells were incubated at 37 °C under a CO_2 concentration of 5% and humidity of 95%. Subcultures were performed at approximately 80–90% confluence. All samples were sterilized through Co-60 irradiation and scaffold extracts were obtained following ISO 10993-5 guidelines. Considering the lower degradation rate of Mg-based materials in vivo compared to in vitro conditions, the scaffold extracts were diluted following protocols described in the literature.

The biocompatibility of porous magnesium metal scaffolds was tested on HBMSCs and HUVEC cells using the Cell Counting Kit-8 (CCK-8, **Dojindo**, Japan). HBMSCs were seeded at 2×10^3 cells/well in 96-well plates and HUVEC cells were seeded at 2.5×10^3 cells/well. Scaffold extract was used to replace the culture medium and incubated for 1, 3, and 5 days. At specific time intervals, a 10% volume of CCK-8 solution was added and incubated for further 1.5 h in the cell incubator. Subsequently, 100 μl of the supernatant was collected and its absorbance (OD) at 450 nm was recorded using a microplate reader (**Bio-Tek**, USA).

Cell viability was evaluate using the live/dead staining kit (Beyotime, China). HBMSCs and HUVECs cells were seeded in 24-well plates at a density of 4×10^3 cells/well and 4.5×10^3 cells/well, respectively. After washing three times with PBS solution, the cells were incubated with 500 ul of live/dead staining reagent for 30 min and observed under a fluorescence microscope.

Cell proliferation was evaluated using Ki67 immunostaining. HBMSCs and HUVEC cells were seeded at a density of 3×10^3 cells/well in a 24-well plate. After cell adherence, the medium was replaced with scaffold extract and cultured for 3 days. Samples were then washed with PBS, fixed with 4% paraformaldehyde for 20 min, permeabilized with 0.1% Triton X-100 for 15 min, blocked with goat serum, and incubated overnight at 4 °C with Ki67

antibody (ab15580, **Abcam**), followed by incubation with fluorescently labeled secondary antibody for 1 h. The nuclei were stained with DAPI (**Solarbio**, C0065) and analyzed using a fluorescence microscope. All experiments were performed in triplicate.

Cell morphology on the surface of JDBM/SrOCP scaffolds

Since the JDBM scaffold exhibited gas production when immersed in vitro, it hindered cell adhesion on its surface. Therefore, HBMSCs were seeded onto the surface of the JDBM/SrOCP scaffold to investigate its morphological characteristics. The seeding density of HBMSCs was 2×10^5 cells/ml. Following a direct co-culture for 5 days, the cells were washed twice with PBS and then fixed in 2.5% glutaraldehyde at 4℃ for over 4 h. Subsequently, they were washed twice with PBS for 20 min, each time. The cells were sequentially subjected to ethanol dehydration with each step lasting between 20 and 30 min. Finally, samples underwent supercritical drying and were prepared via gold sputtering for 2 min before SEM images were captured to observe cell morphology on the scaffold surface.

Alkaline phosphatase and alizarin red staining

HBMSCs were employed to assess the osteogenic properties of the scaffolds in vitro. HBMSCs were seeded into 24-well plates at a density of 6×10^3 cells per well. Once the cells had fully adhered to the surface, the complete medium was replaced with scaffold extracts prepared using an osteogenic induction medium (**OriCell**, HUXMX-90021). The culture was continued for 7 and 14 days. The alkaline phosphatase staining was performed using a BCIP/NBT staining kit (C3206, **Beyotime**). After co-culturing for 21 days, calcium nodules were stained using alizarin red (ALIR-10001, OriCell). The staining results were examined under a stereomicroscope (DS-Ri2, Nikon).

RT-qPCR

Real-time quantitative polymerase chain reaction (RT-qPCR) was performed to determine the expression of osteogenic genes alkaline phosphatase (ALP), collagen type I (COL1), Runt-related transcription factor 2 (RUNX2), osteocalcin (OCN), and angiogenic genes platelet endothelial cell adhesion molecule (CD31) and vascular endothelial growth factor (VEGF). GAPDH served as the reference gene. Specifically, HBMSCs and HUVECs were seeded into 6-well plates at a density of 2×10^5 cells/well. Once the cells adhered fully, the HBMSCs were replaced with scaffold extract prepared using an osteogenic induction medium, while the HUVECs were replaced with the same scaffold extract. HBMSCs were cultured for 7 and 14 days, while HUVEC cells were cultured for an additional 3 days. Next, total RNA was extracted with the RNA extraction kit (Toyobo, FSQ-201). RT-qPCR analysis was performed using the Takara SYBR® Premix Ex TaqII kit (GenStar, A303) and CFX96 real-time detection system. Each sample was replicated three times to improve accuracy. The primer sequences for all genes are presented in Supplementary Table S1.

Immunofluorescence staining

The HBMSCs were cultured using the indirect contact method. They were seeded in 24-well plates at a density of 2×10^3 cells/well. Once the cells had fully adhered, they were replaced with the scaffold extract collected from the osteogenic induction medium. The cells were fixed with 4% paraformaldehyde for 20 min at specific time points, washed with PBS solution, treated with 0.1% Triton X-100 for 15 min, and washed with PBS. They were then blocked with goat serum, and incubated with the Runt-related transcription factor 2 (RUNX2, ab192256, Abcam,1: 200), type I collagen (COL1, ab138492, Abcam,1:100), osteopontin (Opn, ab63856, Abcam,1:100), osteocalcin (OCN,23418-1-AP, Proteintech,1:100), overnight at 4 °C. All samples were incubated with fluorescently labeled secondary antibodies for 1 h, nuclei were labeled with DAPI (Solarbio, C0065), washed three times with PBS, and examined under a fluorescence microscope in triplicate.

Scratch test

The culture of HUVECs was conducted using the indirect contact method. The cells were subsequently seeded on a 6-well plate at a density of 4×10^5 cells per well. Once the HUVEC reached the target confluence, a vertical scratch was made in the center of each well using a 200 uL pipet tip. After thorough washing with sterile PBS, any detached cells were removed, and ECM endothelial cell medium without serum was added. Images were taken at 0 and 24 h post-scratching, and the extent of scratch closure was quantified using ImageJ software.

Transwell assay

The transwell chambers were placed in 24-well plates and divided into three groups, each with three wells. Chambers for the blank group were added with 600 μl of ECM endothelial cell low serum medium, while the JDBM and JDBM/SrOCP groups were treated with 600 μl of ECM endothelial cell low serum medium containing the extract, respectively. The upper chamber was supplemented with 200 μl suspension containing 2×10^4 HUVEC cells and cultured for 24 h. After gently scraping off any remaining cells from the upper layer, the lower layer of the chamber was fixed with 4% paraformaldehyde for 20 min. Subsequently, staining with a 0.1% crystal violet solution (Solarbio, G1063) was carried out for 30 min. Cell migration events were observed using a

light microscope (Ni-U, Nikon, Japan), and the number of migrated HUVEC cells was quantified using ImageJ software.

Tube formation investigation of scaffolds

Angiogenesis assays were performed using Matrigel (Corning, 354234) in ibidi μslide Angiogenesis plates. Specifically, the ibidi angiogenesis specific well plates were coated with Matrigel and HUVECs were suspended in ECM endothelial cell medium, JDBM scaffold extract, and JDBM/SrOCP scaffold extract. A 50 ul cell suspension containing 1×10^4 HUVECs was seeded on the ibidi plates. After a cultivation period of 6 h, tube formation was observed and captured using a light microscope (Ni-U, Nikon, Japan). The tube formation was quantitatively analyzed using ImageJ software. Key parameters measured comprised total tube length, number of nodes, and number of junctions.

Transcriptomic assay

In summary, HBMSCs were lysed using TRIzol reagent, and the total RNA was extracted for library construction, transcriptome data collection, and analysis by Novogene Co., Ltd (Beijing, China). The quality and quantity of the RNA were assessed with an Agilent 2100 Bioanalyzer. It was then sequenced on the Illumina NovaSeq 6000 platform. DESeq2 software (version 1.20.0) was used for gene expression quantification and differential gene expression analysis between the two comparison groups. To investigate functional annotations of differentially expressed genes, cluster profile software (version 3.8.1) was employed for GO (Gene Ontology) and KEGG pathway enrichment analyses.

In vivo experiments

Bone repair assessment in vivo

The experimental protocol was approved by the Experimental Animal Ethics Committee of the Chinese PLA General Hospital (approval number: S2020-169-01). A rat femoral condyle defect model was established to validate the scaffold's in vivo osteogenic and angiogenic capabilities. Eight-week-old male Sprague Dawley (SD) rats ($n = 54$, 280–320 g) were intraperitoneally anesthetized with sodium pentobarbital at a dosage of 30 mg/kg. In a sterile environment, a longitudinal incision was created in the medial distal femur to expose the medial femoral condyle. Next, a cylindrical bone defect with dimensions of 2.6 mm in diameter and 2.8 mm in depth was generated by drilling into the medial femoral condyle using a 2.6 mm drill. The scaffolds were implanted into the defect, and after achieving sufficient hemostasis, the surgical site was meticulously sutured layer by layer. Subsequently, the wound was sterilized using iodophor. The rats were randomly divided into three groups: blank group ($n = 18$), JDBM group ($n = 18$), and JDBM/SrOCP group ($n = 18$).

Vascular perfusion

To observe early revascularization after scaffold implantation, we conducted microvascular perfusion at 4 and 8 weeks after scaffold implantation. Three rats were randomly selected from each group and at each time point. After anesthesia, the rats were positioned supine on a plate and a midline incision was made through the abdomen's epidermis and muscle layer. The xiphoid process was elevated to access the thoracic cavity by cutting through the diaphragm and sternum. Subsequently, an infusion needle was inserted approximately 2 mm deep into the left ventricle while simultaneously severing the inferior vena cava. Following euthanasia, the rats were perfused with normal saline (containing 500 U/L heparin) until the venous outflow changed from red to colorless normal saline. Subsequently, paraformaldehyde fixative was continuously perfused until the lower limbs and tail of the rats trembled. Following the MICROFIL® perfusion solution instructions, the syringe was manually pushed until the blood vessels of vital organs such as the liver, kidneys, and mesentery in the rat's body gradually turned yellow, indicating successful perfusion. The samples were stored in a refrigerator overnight at 4° C to allow full solidification and decalcification after sampling.

Micro-CT assessment

The samples were collected at 4, 8, and 12 weeks post-surgery. Immediately after collection, they were fully fixed using a 4% paraformaldehyde solution and then underwent MicroCT scanning (Belgium, Bruker, Skyscan1276) at a spatial resolution of 13 μm for three-dimensional reconstruction. A ray source voltage of 85 kV, current of 160 μA, and scan rotation angle of 360° were used. The region of interest for all samples was defined as a cylindrical volume with a diameter of 2.6 mm and a height of 2.8 mm. Bone morphometric parameters, including bone volume/total tissue volume (Bv/Tv), trabecular number (Tb. N), trabecular spacing (Tb.Sp), trabecular thickness (Tb. Th), Bone mineral density measurements (BMD), and vascular volume fraction (BVV/TV) were calculated. All samples were collected in triplicate.

Hard tissue section

The EXAKT system was employed to prepare hard tissue sections. Rat femora were subjected to gradient ethanol dehydration and then embedded in light-cured resin. Sections with a thickness of 200 μm were collected using the E300CP hard tissue slicing machine (EXAKT, Germany) and then polished on a grinder to obtain a thickness range of 25 to 35 μm. Microscopic observation was

performed using Goldner trichrome staining (Solarbio, G3550).

Histological tests and immunohistochemical analysis

Histology and immunohistochemistry techniques were employed to assess early vascularized bone regeneration ability of the scaffold after 4 weeks of implantation. Bone tissue samples were fixed using 4% paraformaldehyde, decalcified in 10% ethylenediamine tetraacetic acid (EDTA), embedded in paraffin, sectioned at a thickness of 5 μm, and stained with hematoxylin and eosin (HE). To perform immunohistochemical staining, sections were deparaffinized and subjected to antigen retrieval using 3% hydrogen peroxide (H_2O_2) and pepsin (Abcam, ab64201). Next, the sections were treated with 0.1% Triton X-100 for 15 min and blocked with 10% goat serum. They were then incubated with Osteopontin (Opn, ab63856,Abcam,1:100), osteocalcin (OCN,23418-1-AP, Proteintech, 1:100), CD31 (ab182981,abcam,1:100) and EMCN (sc-65495,Santa Cruz,1:200) overnight at 4° C and at room temperature for 1 h with the secondary antibody. Finally, they were analyzed with a light microscope using the DBA chromogenic substrate system. Immunofluorescence staining was conducted using a protocol similar to that of immunohistochemistry. The primary antibody was incubated overnight at 4 °C, and then washed three times with PBS. Subsequently, the samples were incubated with the secondary antibody (AB150077, Abcam, 1:200) at room temperature. Nuclear staining was performed using DAPI. Images were captured with a fluorescence microscope, and the immunofluorescence intensity was quantified using ImageJ software. All experiments were performed in triplicate.

Statistical analysis

All experiments were repeated three times. Statistical analysis and graphs were performed using GraphPad Prism 9.4 software. All data are presented as the mean ± standard deviation (SD). Student's t-test was employed to compare two groups, and one-way analysis of variance (ANOVA) was used to compare multiple groups. The difference was considered to be statistically significant at $P < 0.05$.

Supplementary Information

The online version contains supplementary material available at https://doi.org/10.1186/s12951-025-03222-3 .

Supplementary Material 1

Supplementary Material 2

Supplementary Material 3

Acknowledgements

The authors thank Guangyin Yuan and Jiang Peng for their valuable comments and suggestions.

Author contributions

Jianting Ye: Conceptualization, Investigation, Data curation, Writing – original draft.Bozun Miao: Conceptualization, Methodology, Investigation, Writing – review & editing. Yingjie Xiong: Conceptualization, Methodology, Writing – review & editing. Yanjun Guan: Conceptualization, Writing – review & editing. Yuzheng Lu: Supervision, Writing – review & editing. Zhibo Jia: Formal analysis, Validation. Yanbin Wu: Resources, Investigation. Xiaohan Sun: Investigation, Writing–review & editing.Congcong Guan: Investigation, Validation, Visualization. Ruichao He: Formal analysis. Xing Xiong: Formal analysis. Huihui Jia: Methodology, Validation. Hongyu Jiang: Validation, Visualization.Zexian Liu: Validation.Yuxuan Zhang: Validation. Yu Wei: Methodology, Software. Wancheng Lin: Resources, Validation.Aiyuan Wang: Investigation.Yu Wang: Investigation.Haoye Meng: Validation.Wenjing Xu: Supervision.Guangyin Yuan: Data curation, Funding acquisition, Project administration, Resources, Supervision, Writing – original draft.Jiang Peng: Data curation, Funding acquisition, Project administration, Resources, Supervision, Writing - review & editing.

Funding

This work was supported by Beijing-Tianjin-Hebei Basic Research Cooperation Program (22JCZXJC00130), National Natural Science Foundation of China Key Program (52130104), National Key Research and Development Program of China (2023YFC2412303), National Natural Science Foundation of China (81972047).

Data availability

All data needed to support the conclusions are present in the paper or the additional materials.

Declarations

Ethics approval and consent to participate

The experimental protocol was approved by the Experimental Animal Ethics Committee of the Chinese PLA General Hospital (approval number: S2020-169-01).

Consent for publication

All authors agree to publication.

Competing interests

The authors declare no competing interests.

Author details

[1]Institute of Orthopedics,The Fourth Medical Center of Chinese PLA General Hospital, Beijing Key Lab of Regenerative Medicine in Orthopedics, Key Laboratory of Musculoskeletal Trauma & War Injuries PLA, No. 51 Fucheng Road, Beijing 100048, PR China
[2]National Engineering Research Center of Light Alloy Net Forming and State Key Laboratory of Metal Matrix Composite School of Materials Science and Engineering, Shanghai Jiao Tong University, Shanghai 200240, China
[3]Department of Spine Surgery, Beijing Shijitan Hospital, Capital Medical University, No.10 Tieyi Road,Haidian District, Beijing 100038, PR China
[4]Hebei North University, Zhangjiakou 075051, PR China
[5]School of Medicine, Nankai University, Tianjin 300071, PR China
[6]Shanxi Provincial People's Hospital, Taiyuan, Shanxi 030012, China

Received: 4 October 2024 / Accepted: 10 February 2025
Published online: 03 March 2025

References

1. Zhang J, He F, Zhang W, Zhang M, Yang H, Luo Z-P. Mechanical force enhanced bony formation in defect implanted with calcium sulphate cement. Bone Res. 2015;3:14048.

2. Hoffman MD, Xie C, Zhang X, Benoit DSW. The effect of mesenchymal stem cells delivered via hydrogel-based tissue engineered periosteum on bone allograft healing. Biomaterials. 2013;34:8887–98.
3. Putelli C, Pilli J, Gatto G, Bhattacharjee A. Tannic acid-loaded MgO and ZnO-Doped Antibacterial Hydroxyapatite for Orthopedic and Dental Applications. Jom. 2024;76:5703–12.
4. Liu S, Han Z, Hao J-N, Zhang D, Li X, Cao Y, Huang J, Li Y. Engineering of a NIR-activable hydrogel-coated mesoporous bioactive glass scaffold with dual-mode parathyroid hormone derivative release property for angiogenesis and bone regeneration. Bioactive Mater. 2023;26:1–13.
5. Meng H, Liu X, Liu R, Zheng Y, Hou A, Liu S, He W, Wang Y, Wang A, Guo Q, Peng J. Decellularized laser micro-patterned osteochondral implants exhibit zonal recellularization and self-fixing for osteochondral regeneration in a goat model. J Orthop Translation. 2024;46:18–32.
6. Fang H, Zhu D, Yang Q, Chen Y, Zhang C, Gao J, Gao Y. Emerging zero-dimensional to four-dimensional biomaterials for bone regeneration. J Nanobiotechnol. 2022;20:26.
7. Sohn H-S, Oh J-K. Review of bone graft and bone substitutes with an emphasis on fracture surgeries. Biomaterials Res. 2019;23:9.
8. Shi H, Zhou K, Wang M, Wang N, Song Y, Xiong W, Guo S, Yi Z, Wang Q, Yang S. Integrating physicomechanical and biological strategies for BTE: biomaterials-induced osteogenic differentiation of MSCs. Theranostics. 2023;13:3245–75.
9. Deng C, Zhou Q, Zhang M, Li T, Chen H, Xu C, Feng Q, Wang X, Yin F, Cheng Y, Wu C. Bioceramic scaffolds with antioxidative functions for ROS scavenging and Osteochondral Regeneration. Adv Sci. 2022;9:2105727.
10. Bohara S, Suthakorn J. Surface coating of orthopedic implant to enhance the osseointegration and reduction of bacterial colonization: a review. Biomaterials Res. 2022;26:26.
11. Jia B, Yang H, Zhang Z, Qu X, Jia X, Wu Q, Han Y, Zheng Y, Dai K. Biodegradable Zn–Sr alloy for bone regeneration in rat femoral condyle defect model: in vitro and in vivo studies. Bioactive Mater. 2021;6:1588–604.
12. Guo T, Scimeca J-C, Ivanovski S, Verron E, Gulati K. Enhanced Corrosion Resistance and local therapy from Nano-Engineered Titanium Dental implants. Pharmaceutics. 2023;15:315.
13. Koons GL, Diba M, Mikos AG. Materials design for bone-tissue engineering. Nat Reviews Mater. 2020;5:584–603.
14. Meng H, Quan Q, Yuan X, Zheng Y, Peng J, Guo Q, Wang A, Lu S. Diffusion of neutral solutes within human osteoarthritic cartilage: effect of loading patterns. J Orthop Translation. 2020;22:58–66.
15. Zhang Z, Li Z, Zhang C, Liu J, Bai Y, Li S, Zhang C. Biomimetic intrafibrillar mineralized collagen promotes bone regeneration via activation of the wnt signaling pathway. Int J Nanomed. 2018;13:7503–16.
16. Ge YW, Liu XL, Yu DG, Zhu ZA, Ke QF, Mao YQ, Guo YP, Zhang JW. Graphene-modified CePO4 nanorods effectively treat breast cancer-induced bone metastases and regulate macrophage polarization to improve osteo-inductive ability. J Nanobiotechnol. 2021;19:11.
17. Wei X, Zhou W, Tang Z, Wu H, Liu Y, Dong H, Wang N, Huang H, Bao S, Shi L, et al. Magnesium surface-activated 3D printed porous PEEK scaffolds for in vivo osseointegration by promoting angiogenesis and osteogenesis. Bioact Mater. 2023;20:16–28.
18. Kim J-W, Han Y-S, Lee H-M, Kim J-K, Kim Y-J. Effect of morphological characteristics and biomineralization of 3D-Printed Gelatin/Hyaluronic Acid/Hydroxyapatite composite scaffolds on bone tissue regeneration. Int J Mol Sci. 2021;22:6794.
19. Wang W, Xiong Y, Zhao R, Li X, Jia W. A novel hierarchical biofunctionalized 3D-printed porous Ti6Al4V scaffold with enhanced osteoporotic osseointegration through osteoimmunomodulation. J Nanobiotechnol. 2022;20:68.
20. Qiao W, Wong KHM, Shen J, Wang W, Wu J, Li J, Lin Z, Chen Z, Matinlinna JP, Zheng Y, et al. TRPM7 kinase-mediated immunomodulation in macrophage plays a central role in magnesium ion-induced bone regeneration. Nat Commun. 2021;12:2885.
21. Li H, Arculus RJ, Ishizuka O, Hickey-Vargas R, Yogodzinski GM, McCarthy A, Kusano Y, Brandl PA, Savov IP, Tepley FJ, Sun W. Basalt derived from highly refractory mantle sources during early Izu-Bonin-Mariana arc development. Nat Commun. 2021;12:1723.
22. Wang J, Witte F, Xi T, Zheng Y, Yang K, Yang Y, Zhao D, Meng J, Li Y, Li W, et al. Recommendation for modifying current cytotoxicity testing standards for biodegradable magnesium-based materials. Acta Biomater. 2015;21:237–49.
23. Lin S, Yang G, Jiang F, Zhou M, Yin S, Tang Y, Tang T, Zhang Z, Zhang W, Jiang X. A magnesium-enriched 3D culture system that mimics the Bone Development Microenvironment for Vascularized Bone Regeneration. Adv Sci (Weinh). 2019;6:1900209.
24. Xu H, Tian F, Liu Y, Liu R, Li H, Gao X, Ju C, Lu B, Wu W, Wang Z, et al. Magnesium malate-modified calcium phosphate bone cement promotes the repair of vertebral bone defects in minipigs via regulating CGRP. J Nanobiotechnol. 2024;22:368.
25. Wu S, Chen Z, Yu X, Duan X, Chen J, Liu G, Gong M, Xing F, Sun J, Huang S, Xiang Z. A sustained release of BMP2 in urine-derived stem cells enhances the osteogenic differentiation and the potential of bone regeneration. Regenerative Biomaterials. 2022;9:rbac015.
26. Kang YG, Wei J, Shin JW, Wu YR, Su J, Park YS, Shin J-W. Enhanced biocompatibility and osteogenic potential of mesoporous magnesium silicate/polycaprolactone/wheat protein composite scaffolds. Int J Nanomed. 2018;13:1107–17.
27. Wang JL, Xu JK, Hopkins C, Chow DH, Qin L. Biodegradable magnesium-based implants in Orthopedics-A General Review and perspectives. Adv Sci (Weinh). 2020;7:1902443.
28. Ma D, Wang J, Zheng M, Zhang Y, Huang J, Li W, Ding Y, Zhang Y, Zhu S, Wang L, et al. Degradation behavior of ZE21C magnesium alloy suture anchors and their effect on ligament-bone junction repair. Bioactive Mater. 2023;26:128–41.
29. Ma Z, Liu B, Li S, Wang X, Li J, Yang J, Tian S, Wu C, Zhao D. A novel biomimetic trabecular bone metal plate for bone repair and osseointegration. Regenerative Biomaterials. 2023;10:rbad003.
30. Grigore TV, Zuidscherwoude M, Witasp A, Barany P, Wernerson A, Bruchfeld A, Xu H, Olauson H, Hoenderop J. Fibroblast growth factor 23 is independently associated with renal magnesium handling in patients with chronic kidney disease. Front Endocrinol. 2023;13:1046392.
31. Lai Y, Li Y, Cao H, Long J, Wang X, Li L, Li C, Jia Q, Teng B, Tang T, et al. Osteogenic magnesium incorporated into PLGA/TCP porous scaffold by 3D printing for repairing challenging bone defect. Biomaterials. 2019;197:207–19.
32. Cihova M, Martinelli E, Schmutz P, Myrissa A, Schäublin R, Weinberg AM, Uggowitzer PJ, Löffler JF. The role of zinc in the biocorrosion behavior of resorbable Mg–Zn–Ca alloys. Acta Biomater. 2019;100:398–414.
33. Pachla W, Przybysz S, Jarzębska A, Bieda M, Sztwiertnia K, Kulczyk M, Skiba J. Structural and mechanical aspects of hypoeutectic Zn–Mg binary alloys for biodegradable vascular stent applications. Bioactive Mater. 2021;6:26–44.
34. Du S, Shen Y, Zheng Y, Cheng Y, Xu X, Chen D, Xia D. Systematic in vitro and in vivo study on biodegradable binary Zn-0.2 at% Rare Earth alloys (Zn-RE: sc, Y, La–Nd, Sm–Lu). Bioactive Mater. 2023;24:507–23.
35. Sahu MR, Kumar TSS, Chakkingal U. A review on recent advancements in biodegradable Mg-Ca alloys. J Magnesium Alloys. 2022;10:2094–117.
36. Wang Y, Liu B, Zhao X, Zhang X, Miao Y, Yang N, Yang B, Zhang L, Kuang W, Li J, et al. Turning a native or corroded mg alloy surface into an anti-corrosion coating in excited CO(2). Nat Commun. 2018;9:4058.
37. Park SS, Farwa U, Park I, Moon BG, Im SB, Lee BT. In-vivo bone remodeling potential of Sr-d-Ca-P /PLLA-HAp coated biodegradable ZK60 alloy bone plate. Mater Today Bio. 2023;18:100533.
38. Cui L-Y, Cheng S-C, Liang L-X, Zhang J-C, Li S-Q, Wang Z-L, Zeng R-C. In vitro corrosion resistance of layer-by-layer assembled polyacrylic acid multilayers induced Ca–P coating on magnesium alloy AZ31. Bioactive Mater. 2020;5:153–63.
39. Su Y, Wang K, Gao J, Yang Y, Qin Y-X, Zheng Y, Zhu D. Enhanced cytocompatibility and antibacterial property of zinc phosphate coating on biodegradable zinc materials. Acta Biomater. 2019;98:174–85.
40. Mardali M, Salimijazi H, Karimzadeh F, Blawert C, Luthringer-Feyerabend BJC, Fazel M, Safarbali B. Microstructure and corrosion characterization of a MgO/Hydroxyapatite bilayer coating by plasma electrolytic oxidation coupled with flame spraying on a mg alloy. ACS Omega. 2020;5:24186–94.
41. Zhang N, Wang W, Zhang X, Nune KC, Zhao Y, Liu N, Misra RDK, Yang K, Tan L, Yan J. The effect of different coatings on bone response and degradation behavior of porous magnesium-strontium devices in segmental defect regeneration. Bioact Mater. 2021;6:1765–76.
42. Khadem SA, Bagnani M, Mezzenga R, Rey AD. Relaxation dynamics in biocolloidal cholesteric liquid crystals confined to cylindrical geometry. Nat Commun. 2020;11:4616.
43. Liu Y, Yang Z, Wang L, Sun L, Kim BYS, Jiang W, Yuan Y, Liu C. Spatiotemporal Immunomodulation using Biomimetic Scaffold promotes endochondral ossification-mediated Bone Healing. Adv Sci. 2021;8:202100143.
44. Wallat L, Altschuh P, Reder M, Nestler B, Poehler F. Computational design and characterisation of Gyroid structures with different gradient functions for Porosity Adjustment. Materials. 2022;15:3730.

45. Yang Y, Xu T, Bei H-P, Zhang L, Tang C-Y, Zhang M, Xu C, Bian L, Yeung KW-K, Fuh JYH, Zhao X. Gaussian curvature–driven direction of cell fate toward osteogenesis with triply periodic minimal surface scaffolds. *Proceedings of the National Academy of Sciences* 2022, 119.
46. Li X, Gao P, Wan P, Pei Y, Shi L, Fan B, Shen C, Xiao X, Yang K, Guo Z. Novel bio-functional Magnesium Coating on Porous Ti6Al4V Orthopaedic implants: in vitro and in vivo study. Sci Rep. 2017;7:40755.
47. Zhang Y, Lin T, Meng H, Wang X, Peng H, Liu G, Wei S, Lu Q, Wang Y, Wang A, et al. 3D gel-printed porous magnesium scaffold coated with dibasic calcium phosphate dihydrate for bone repair in vivo. J Orthop Translat. 2022;33:13–23.
48. Wang W, Jia G, Wang Q, Huang H, Li X, Zeng H, Ding W, Witte F, Zhang C, Jia W, Yuan G. The in vitro and in vivo biological effects and osteogenic activity of novel biodegradable porous mg alloy scaffolds. Mater Design 2020, 189.
49. Hu H, Zhao P, Liu J, Ke Q, Zhang C, Guo Y, Ding H. Lanthanum phosphate/chitosan scaffolds enhance cytocompatibility and osteogenic efficiency via the Wnt/β-catenin pathway. J Nanobiotechnol. 2018;16:98.
50. Qiu M, Li C, Cai Z, Li C, Yang K, Tulufu N, Chen B, Cheng L, Zhuang C, Liu Z, et al. 3D biomimetic calcified cartilaginous callus that induces type H vessels formation and Osteoclastogenesis. Adv Sci. 2023;10:202207089.
51. Qiao W, Pan D, Zheng Y, Wu S, Liu X, Chen Z, Wan M, Feng S, Cheung KMC, Yeung KWK, Cao X. Divalent metal cations stimulate skeleton interoception for new bone formation in mouse injury models. Nat Commun. 2022;13:535.
52. Lee MS, Jeon J, Park S, Lim J, Yang HS. Rationally designed bioactive milk-derived protein scaffolds enhanced new bone formation. Bioactive Mater. 2023;20:368–80.
53. Nie W, Gao Y, McCoul DJ, Gillispie GJ, Zhang Y, Liang L, He C. Rapid mineralization of hierarchical poly(l-lactic acid)/poly(ε-caprolactone) nanofibrous scaffolds by electrodeposition for bone regeneration. Int J Nanomed. 2019;14:3929–41.<\/p>
54. Tu B, Liu S, Yu B, Zhu J, Ruan H, Tang T, Fan C. miR-203 inhibits the traumatic heterotopic ossification by targeting Runx2. Cell Death Dis. 2016;7:e2436–2436.
55. Zhang Y, Li Y, Liao W, Peng W, Qin J, Chen D, Zheng L, Yan W, Li L, Guo Z, et al. Citrate-stabilized Gold Nanorods-Directed osteogenic differentiation of multiple cells. Int J Nanomed. 2021;16:2789–801.
56. Perez JE, Bajaber B, Alsharif N, Martínez-Banderas AI, Patel N, Sharip A, Di Fabrizio E, Merzaban J, Kosel J. Modulated nanowire scaffold for highly efficient differentiation of mesenchymal stem cells. J Nanobiotechnol. 2022;20:282.
57. Wu C-Y, Wu T-Y, Guan Z-Y, Wang P-Y, Yang Y-C, Huang C-W, Lin T-H, Chen H-Y. Vapor-phased fabrication and modulation of cell-laden scaffolding materials. Nat Commun. 2021;12:3413.
58. Matsubara T, Iga T, Sugiura Y, Kusumoto D, Sanosaka T, Tai-Nagara I, Takeda N, Fong G-H, Ito K, Ema M, et al. Coupling of angiogenesis and odontogenesis orchestrates tooth mineralization in mice. J Exp Med. 2022;219:e20211789.
59. Wang G, Lv Z, Wang T, Hu T, Bian Y, Yang Y, Liang R, Tan C, Weng X. Surface functionalization of Hydroxyapatite scaffolds with MgAlEu-LDH nanosheets for High-Performance Bone Regeneration. Adv Sci. 2022;10:202204234.
60. Gao P, Fan B, Yu X, Liu W, Wu J, Shi L, Yang D, Tan L, Wan P, Hao Y, et al. Bio-functional magnesium coated Ti6Al4V scaffold enhances osteogenesis and angiogenesis in vitro and in vivo for orthopedic application. Bioactive Mater. 2020;5:680–93.
61. Xu D, Gan K, Wang Y, Wu Z, Wang Y, Zhang S, Peng Y, Fang X, Wei H, Zhang Y, et al. A Composite Deferoxamine/Black Phosphorus Nanosheet/Gelatin Hydrogel Scaffold for ischemic tibial bone repair. Int J Nanomed. 2022;17:1015–30.
62. Chang S, Wang S, Liu Z, Wang X. Advances of stimulus-responsive hydrogels for bone defects repair in tissue Engineering. Gels. 2022;8:389.
63. Zhao Z, Li G, Ruan H, Chen K, Cai Z, Lu G, Li R, Deng L, Cai M, Cui W. Capturing Magnesium ions via Microfluidic Hydrogel Microspheres for promoting Cancellous Bone Regeneration. ACS Nano. 2021;15:13041–54.

Publisher's note